

AMERICAN UNIVERSITY OF BEIRUT

DESIGN AND MODELING OF A NOVEL  
SINGLE-ACTUATOR DIFFERENTIALLY  
DRIVEN ROBOT

by

JOY GEORGE SFEIR

A thesis  
submitted in partial fulfillment of the requirements  
for the degree of Master of Engineering  
to the Department of Mechanical Engineering  
of the Faculty of Engineering and Architecture  
at the American University of Beirut

Beirut, Lebanon  
April 2014

AMERICAN UNIVERSITY OF BEIRUT

DESIGN AND MODELING OF A NOVEL  
SINGLE-ACTUATOR DIFFERENTIALLY  
DRIVEN ROBOT

by  
JOY GEORGE SFEIR

Approved by:

---

Dr. Elie Shamma, Assistant Professor

Advisor

Mechanical Engineering

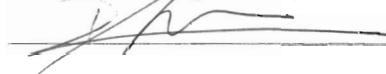


---

Dr. Daniel Asmar, Assistant Professor

Member of Committee

Mechanical Engineering

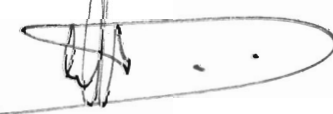


---

Dr. Imad Elhajj, Associate Professor

Member of Committee

Electrical And Computer Engineering



Date of thesis defense: April 29, 2014



# Acknowledgements

Foremost, I would like to express my sincere gratitude to my advisor Dr. Elie Shamma for his guidance, patience, consistent assistance and constructive comments during this academic endeavor.

I would like also to thank Dr. Daniel Asmar for his help, support and his constructive comments in writing papers. I also express my thanks to Dr. Imad Elhajj for extending his support.

I would like also to express my thanks and appreciation to my lab colleagues Bilal Wehbe, Wael Salem, Salah Bazzi, Jean Lahoud and Joseph Saad for their help and support.

My sincere gratitude is hereby extended to my family, friends and whoever gave me support and encouragement during my graduate studies and helped me in fulfilling this thesis work.

# An Abstract of the Thesis of

Joy George Sfeir for Master of Engineering  
Major: Mechanical Engineering

Title: Design and Modeling of a Novel Single-Actuator Differentially Driven Robot

In this thesis, we introduce a concept design for a single-actuator differentially driven robot. The design is based on connecting two variable-diameter wheels to the same drive shaft. The wheels are designed to have engineered stiffness so that the diameters of the wheels are varied by shifting the weight of the drive mechanism from side to side. Hence, as one wheel decreases in diameter and the other increases, the robot steers in the direction of the wheel with the smaller diameter. Moreover, we develop the kinetostatic model of the mobile platform, and show that the system can be simplified and modeled as a vertical rolling disk having a constant radius with a pendulum acting as the driving force. Then, the dynamic analysis of the robot is developed and the equations of motion are derived. Finally, the motion planning problem is studied by applying Dubins curve, and a comparison is made between the real dubins curve obtained for the robot and the perfect dubins curve.

# Contents

<b>Acknowledgements</b>	<b>v</b>
<b>Abstract</b>	<b>vi</b>
<b>List of Figures</b>	<b>ix</b>
<b>List of Tables</b>	<b>xi</b>
<b>1 Introduction</b>	<b>1</b>
1.1 Mobile Wheeled Pendulum . . . . .	1
1.2 Differentially Driven Robots . . . . .	3
1.3 Variable-Diameter Wheels . . . . .	5
1.4 Related Work . . . . .	6
1.5 Thesis Contribution . . . . .	12
1.6 Thesis Outline . . . . .	12
<b>2 Model Design</b>	<b>13</b>
2.1 Model parts . . . . .	13
2.2 The operating mechanism . . . . .	16
<b>3 Kinetostatic Analysis</b>	<b>18</b>
3.1 Kinetostatic Model . . . . .	18
3.2 Simulations and Results . . . . .	20
3.3 Parameters Analysis . . . . .	24
<b>4 Dynamic Analysis</b>	<b>28</b>
4.1 Dynamic Model . . . . .	28
4.2 Simulations and Results . . . . .	31
<b>5 Motion Planning</b>	<b>33</b>
5.1 Perfect Dubins Curve . . . . .	34
5.2 Real Dubins Curve . . . . .	36
5.2.1 Calculating the Function $d(t)$ . . . . .	36
5.2.2 Simplified Dynamic Model . . . . .	36

5.2.3 Simulations and Results . . . . .	38
<b>6 Conclusion</b>	<b>45</b>
<b>A Abbreviations</b>	<b>46</b>
<b>B Design Drawings</b>	<b>47</b>
<b>Bibliography</b>	<b>57</b>

# List of Figures

1.1	Different examples of MWP robots. . . . .	2
1.2	An example of the mobility direction of a differentially driven robot. . . . .	3
1.3	Two types of omni wheels. . . . .	4
1.4	The kuka robot. [1]. . . . .	4
1.5	Different examples of differentially driven robots. . . . .	5
1.6	A wheel that has a diameter which varies according to the resistant torque [2]. . . . .	6
1.7	The IMPASS robot. . . . .	7
1.8	The IMPASS robot performing a turning maneuver. . . . .	7
1.9	The motors used in the IMPASS robot and their locations. . . . .	8
1.10	Different versions of the Scout robot [3]. . . . .	8
1.11	The two stages of the wheel [4]. . . . .	9
1.12	The Foldable Wheel Robot [5]. . . . .	9
1.13	The expendable wheel [6]. . . . .	10
1.14	The expendable wheel robot mechanism [6]. . . . .	10
1.15	The search and rescue robot [7]. . . . .	11
1.16	The search and rescue robot wheel mechanism. . . . .	11
2.1	A mechanical design schematic of the proposed novel robotic platform. . . . .	14
2.2	A detailed view of the transmission system. . . . .	15
2.3	A detailed view of the wheel. . . . .	15
2.4	The pendulum drive mechanism. . . . .	16
2.5	A flow chart describing the method of operation of the robot. . . . .	17
3.1	The kinetostatic Model. . . . .	19
3.2	The effect of variation of $d$ on $r_1$ and $r_2$ with $\gamma = 0$ . . . . .	21
3.3	The effect of $\gamma$ on $r_1$ for different values of $d$ . . . . .	21
3.4	The effect of $\gamma$ on $r_2$ for $d = -0.3m$ . . . . .	22
3.5	The effect of $\gamma$ and $d$ on the height of the center of mass $M_1$ . . . . .	22
3.6	The trajectory followed by the robot for a constant value of $d$ . . . . .	24
3.7	Simulation 1: The effect of changing $\gamma$ on $r_1$ for different values of $\frac{M_1}{M_2}$ at $d = -0.3$ . . . . .	25



3.8	Simulation 2: The effect of changing $\gamma$ on $M_1(z)$ for different values of $\frac{M_1}{M_2}$ at $d = -0.3$ . . . . .	25
3.9	Simulation 3: The effect of changing $\gamma$ on $r_1$ for different values of $\frac{l_s}{r_0}$ at $d = -0.3$ . . . . .	26
3.10	Simulation 4: The effect of changing $\gamma$ on $M_1(z)$ for different values of $\frac{l_s}{r_0}$ at $d = -0.3$ . . . . .	26
3.11	Simulation 5: The effect of changing $\gamma$ on $r_1$ for different values of $\frac{l_p}{r_0}$ at $d = -0.3$ . . . . .	27
3.12	Simulation 6: The effect of changing $\gamma$ on $M_1(z)$ for different values of $\frac{l_p}{r_0}$ at $d = -0.3$ . . . . .	27
4.1	The dynamic Model. . . . .	28
4.2	The trajectories of the robot for different initial conditions and values of $d$ . . . . .	32
5.1	Two examples of Dubins curve: the first has a RSL configuration and the second has a RLR configuration. . . . .	33
5.2	An ideal Dubins curve trajectory with the corresponding step function $d(t)$ . . . . .	35
5.3	The transmission system showing the gears numbers. . . . .	36
5.4	The corresponding function $d(t)$ for the following set of commands: $\frac{\pi}{8}\text{rad}$ , $0.5\text{m}$ , $-\frac{\pi}{8}\text{rad}$ . . . . .	39
5.5	Simulation 1: a comparison showing both the real (top) and perfect (bottom) dubins curves. . . . .	39
5.6	The corresponding function $d(t)$ for the following set of commands: $\frac{\pi}{8}\text{rad}$ , $1.5\text{m}$ , $-\frac{\pi}{8}\text{rad}$ . . . . .	40
5.7	Simulation 2: a comparison showing both the real (top) and perfect (bottom) dubins curves. . . . .	40
5.8	The corresponding function $d(t)$ for the following set of commands: $\frac{\pi}{4}\text{rad}$ , $0.5\text{m}$ , $-\frac{\pi}{4}\text{rad}$ . . . . .	41
5.9	Simulation 3: a comparison showing both the real (top) and perfect (bottom) dubins curves. . . . .	41
5.10	The corresponding function $d(t)$ for the following set of commands: $\frac{\pi}{2}\text{rad}$ , $-\frac{\pi}{2}\text{rad}$ , $\frac{\pi}{2}\text{rad}$ . . . . .	42
5.11	Simulation 4: a comparison showing both the real (top) and perfect (bottom) dubins curves. . . . .	43
5.12	The corresponding function $d(t)$ for the following set of commands: $\frac{\pi}{2}\text{rad}$ , $-\pi\text{rad}$ , $\pi\text{rad}$ . . . . .	43
5.13	Simulation 5: a comparison showing both the real (top) and perfect (bottom) dubins curves. . . . .	44

# List of Tables

1.1	The required directions of the left and right wheels for achieving a particular motion direction in a differentially driven robot. . . .	3
3.1	Simulation Parameters. . . . .	21



# Chapter 1

## Introduction

The objective of this chapter is to give a general overview about some important concepts related to the thesis work. We start by giving an overview about mobile wheeled pendulum (MWP), differentially driven robots, and variable-diameter wheels. Then, we investigate some previous work related to the different types of robots that uses variable-diameter wheels and their designs. Finally, the thesis contributions and outline are presented.

### 1.1 Mobile Wheeled Pendulum

The mobile wheeled pendulum (MWP) comprises two coaxial wheels and an intermediate body. A feature common to this category, that is not encountered in other wheeled robots, is that their central body, which plays the role of the robot platform, can rotate about the wheel axis. This motion should be controlled, thereby leading to a new challenging problem, which is the stabilization of the central body, aside the classical control problem due to nonholonomy [8]. The interest in MWP was promoted by the US patent of the Ginger and the Segway Human Transporter projects. Even though it is pitched as a personal mobility system, the Segway robot has proven to be an effective mobile base that has served the robotics research community. An example of the Segway robot is shown in Fig. 1.1a.

Another MWP example is the JOE robot as shown in Fig. 1.1b. The JOE robot is able to do stationary U-turns due to its configuration with two coaxial wheels, each of which is coupled to a DC Motor [9]. The control system of this robot is made up of two decoupled state-space controllers which pilots the motors in order to maintain the equilibrium of the system.

In 1998, Ostrovskaya and Angeles developed a new class of nonholonomic mechanical systems, known as quasiholonomic, which lies between holonomic and

nonholonomic systems [8]. One example of this class is the Quasimoro robot as shown in Fig. 1.1c. This robot was developed as a service robot for the motion-impaired by Salerno and Angeles in 2004.

Nonholonomic systems are, roughly speaking, mechanical systems with constraints on their velocity that are not derivable from position constraints. They arise, for instance, in mechanical systems that have rolling contact (for example, the rolling of wheels without slipping) or certain kinds of sliding contact (such as the sliding of skates). They are a remarkable generalization of classical Lagrangian and Hamiltonian systems in which one allows position constraints only.



(a) The Segway robot [10].



(b) The JOE robot [9].



(c) Quasimoro, a quasiholonomic mobile robot [8].

Figure 1.1: Different examples of MWP robots.

## 1.2 Differentially Driven Robots

Differential drive is a method for controlling a robot with only two motorized wheels. Differentially driven robots are one of the most popular types of mobile robots. Their configuration consists of two actuated wheels mounted on a common shaft, where each wheel can be independently driven either forwards or backwards. The term "differential" means that robot turning speed is determined by the speed difference between both wheels, each on either sides of the robot. Therefore, changing the relative rate of rotation of the robot's wheels causes a change in its direction. To turn the robot left or right, wheels are rotated at different speeds or in different directions. Table 1.1 and Fig. 1.2 give an example for the direction of the wheels for achieving a particular mobility in a differentially driven robot.

Table 1.1: The required directions of the left and right wheels for achieving a particular motion direction in a differentially driven robot.

Motion	Left Wheel	Right Wheel
Right Turn	Counter Clockwise	Clockwise
Left Turn	Clockwise	Counter Clockwise
Forward	Clockwise	Clockwise
Backward	Counter Clockwise	Counter Clockwise

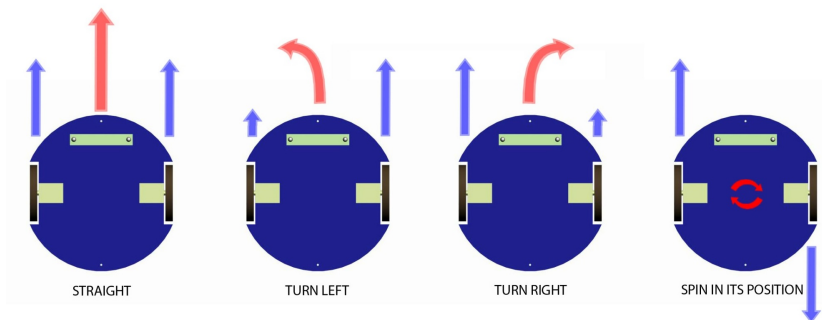


Figure 1.2: An example of the mobility direction of a differentially driven robot.

The example shown in Fig. 1.2, is based on using ordinary wheels which have nonholonomic constraints, meaning that the robot cannot move sideways. But

there exist another type of wheels called the omni wheels, shown in Fig. 1.3, which are wheels with small rolling discs around the circumference that are placed at a certain angle to the rolling direction. These wheels can be controlled differentially to move the robot in almost any direction by rotating each wheel at exactly the right velocity, hence making them ideal for holonomic drive systems. One example of such robot is the kuka robot shown in Fig. 1.4.



(a) A  $90^\circ$  omni wheel. [11].



(b) A  $45^\circ$  omni wheel. [12].

Figure 1.3: Two types of omni wheels.



Figure 1.4: The kuka robot. [1].

Overall, the simplicity of the differential drive approach makes it a very common platform among the robotics community, especially in locomotion systems. Segway robots are one of the best examples [13]. Pioneer, PeopleBot, PowerBot and PatrolBot mobile robots, shown in Fig. 1.10 are also examples of the differentially driven robots.



(a) The Pioneer robot [14].



(b) The PeopleBot robot [15].



(c) The PowerBot robot [16].



(d) The PatrolBot robot [17].

Figure 1.5: Different examples of differentially driven robots.

### 1.3 Variable-Diameter Wheels

The wheeled robot has been mainly designed with a constant diameter wheels. The disadvantage of this design is that the robot can not navigate well over obstacles, such as rocky terrain, sharp declines, or areas with low friction. There exists now an interest for a new type of robot which inherits both advantages of legged and wheeled robots, namely the high adaptive capabilities of legs and the high velocity and payload of the wheels. Therefore, a new approach for tackling the drawbacks of the constant diameter wheels has been adopted by using variable-diameter wheels.



Variable diameter wheel mobile platform could change wheel size according to particular conditions that the robot designer implements. There exists many designs and mechanisms for this new type of wheels in the literature depending on the purpose of use, such as obstacle climbing or driving on rough terrains.

A variable diameter wheel can be controlled in two ways. First, it can be controlled actively, meaning that the wheel is connected directly to an actuator or controller by for example a set of gears and shaft, that can directly change its diameter. Secondly, it can be controlled passively, meaning that the wheel is not connected to an actuator. So in order to change its diameter, the wheel has to be of a spring-type wheel, hence when an external force is applied, the wheel will either fold or unfold. An example of a variable diameter wheel that varies according to the resistant torque is shown in Fig. 1.6.

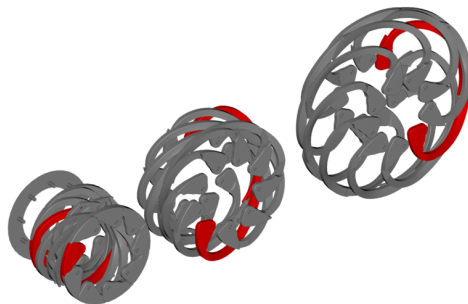


Figure 1.6: A wheel that has a diameter which varies according to the resistant torque [2].

## 1.4 Related Work

In this section, we give an overview of some previous work related to thesis subject.

The intelligent mobility platform with active spoke system (IMPASS) [18] robot shown in Fig. 1.7 is, as far as we know, the only robot that uses variable-diameter wheels for steering. This robot uses a novel method for locomotion which utilizes rimless wheels with individually actuated spokes, therefore, giving it the ability to change its effective diameter on both wheels in order to achieve steering. This form of novel locomotion has the potential to combine the efficiency of a wheeled robot and the mobility of a legged robot. A highly mobile robot such as IMPASS could prove very valuable in applications where the terrain is complex and dangerous, such as search and rescue, reconnaissance, or anti-terror response.

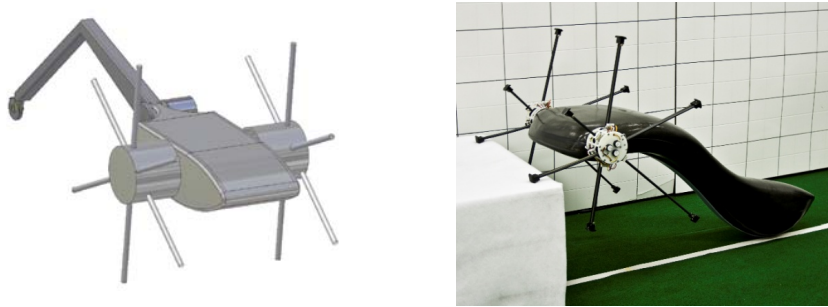


Figure 1.7: The IMPASS robot.

Unlike other wheeled vehicles which use Ackerman steering or differential steering, IMPASS can implement novel turning gaits even though the left and right hubs rotate with the same angular velocity. A constant radius turn for IMPASS is accomplished by using a smaller effective wheel radius for the inside hub, and a larger effective radius for the outside hub, as shown in Fig. 1.8.

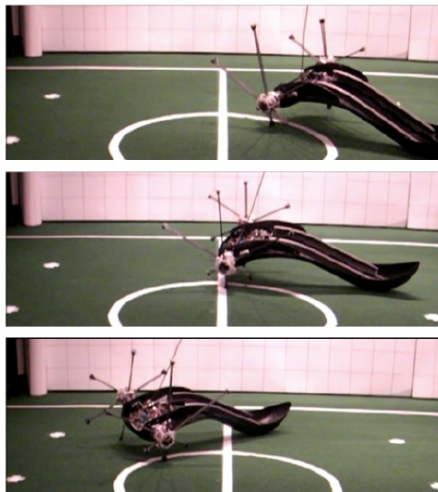


Figure 1.8: The IMPASS robot performing a turning maneuver.

The disadvantage of such a design is that the wheels are modeled as a spoked wheel system which requires an individual motor for each spoke to be actuated, as shown in Fig. 1.9, and thus leads to degradation in efficiency and more complexity.

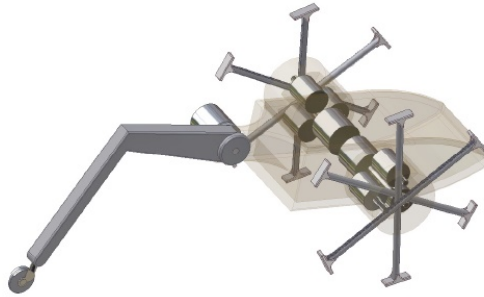


Figure 1.9: The motors used in the IMPASS robot and their locations.

Another type of robot that uses spoked wheels is the Scout robot [19] which has been developed at the University of Minnesota in partnership with MTS, Honeywell, and ATC. Several augmentations to the Scout have been made. Each is an attempt to address a limitation of the standard Scout whether it be locomotion, sensing, or communication. The actuating wheel scout version 1, as shown in Fig. 1.10a, created a wheel system that allowed a dynamic range of wheel diameter from 44 mm to 120 mm, enabling operation on a variety of terrain. Fig. 1.10b, shows the actuating wheel scout version 2 which improved upon the mechanical design of the first version while restoring the launch form factor by enabling a range of 39 mm to 120 mm.



(a) The actuating wheel scout version 1.



(b) The actuating wheel scout version 2.

Figure 1.10: Different versions of the Scout robot [3].

The authors in [20] propose a variable diameter wheel mobile platform which can meet the requirement of travelling on the complex terrain such as mountain, ditches, paddy field, and dry land. Variable diameter wheel and H-drive four-wheel drive system was developed, and transmission ratio was identified. Fig. 1.11 shows a 3D model of the proposed variable diameter wheel.

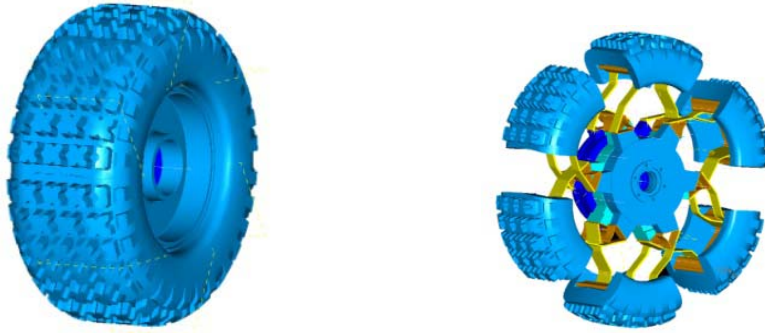


Figure 1.11: The two stages of the wheel [4].

In [21], the authors present a novel high adaptability out-door mobile robot with variable-diameter wheels. The robot is designed for the purpose of climbing obstacles and adapting to different terrain with a self-adapting suspension mechanism, by using a foldable wheel design a shown in Fig. 1.12. The wheel is based on a retractable polyhedron structure with a single degree of freedom, controlled by the rotation of the triangular shaped piece in the center.



Figure 1.12: The Foldable Wheel Robot [5].

The authors in [6] propose an innovative design for a variable-diameter wheel, shown in Fig. 1.13 with an expendable mechanism for unfolding it. This mechanism combines two sub-mechanisms. One allows the deployment of the rim while the other one ensures the contact shape adaptation.

The expansion mechanism is actuated by a rotation of each lateral rim part. Each part is composed of arc-shaped rods which are in contact in the compact form. In this concept, the expansion of the wheel is obtained by a motion of elementary rods constrained in the sagittal plan. The expansion of the rim is based on a three-beam planar mechanism. This mechanism shown in Fig. 1.14 is the elementary mesh that constitute one of two lateral parts of the wheel.

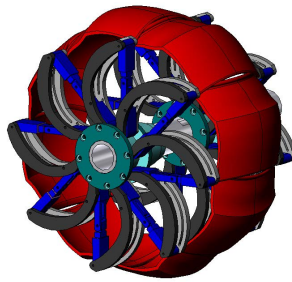


Figure 1.13: The expendable wheel [6].

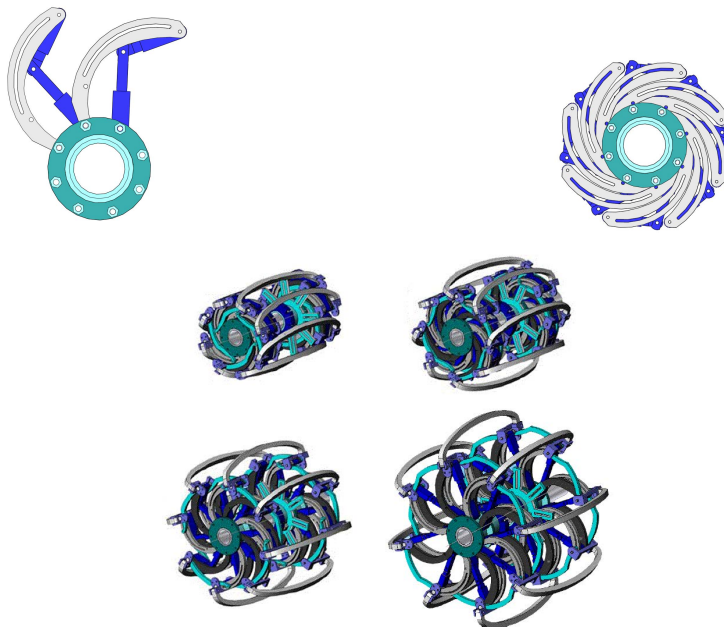


Figure 1.14: The expendable wheel robot mechanism [6].

Another robot that uses variable-diameter wheel is the search and rescue robot developed in [7]. The robot is designed to navigate through wreckage which consists of narrow spaces and large obstacles. In such environments, the robot should have a small size to navigate through narrow spaces, and also have the ability to climb over obstacles. In order to achieve both requirements, the authors developed a transformable mobile robot that can change its wheels' diameters for adapting to various environments as shown in Fig. 1.15.

The mechanism of the variable-diameter wheel is composed of six equally angular-spaced pantographs which transforms horizontal displacement to vertical displacement. A series of motion of one pantograph mechanism is shown in Fig. 1.16. In this figure, the length of the mechanism (vertical direction) is increased while the width between the two disks is decreased. To change the width between the

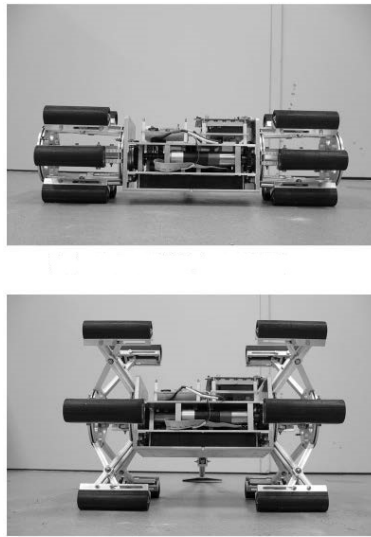


Figure 1.15: The search and rescue robot [7].

two disks, a linear actuator is used which is composed of trapezoidal-screwthread and DC-motor.

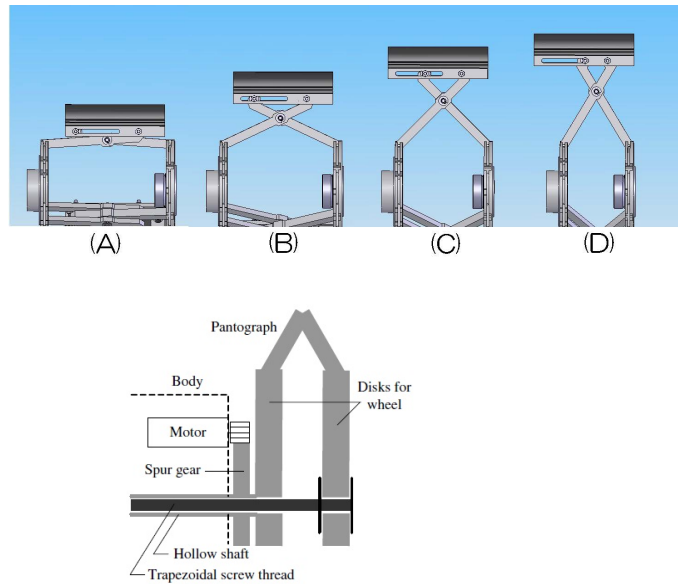


Figure 1.16: The search and rescue robot wheel mechanism.

The designs proposed in [20], [21], [6] and [7] present different types for the variable-diameter wheel, which are controlled actively by transferring part of the actuator energy to directly change the diameter. The drawback of this method

is that it introduces additional complexity and cost to the problem as compared to a passive control mechanism. Additionally, the wheels are designed to vary in the same direction and thus require another mechanism for steering.

## 1.5 Thesis Contribution

In this thesis, we consider the problem of designing a differentially driven robot with a single actuator. The diameters of the wheels of the proposed concept design are controlled passively by shifting the actuator's weight closer to one of the wheels and causing its diameter to decrease while increasing the diameter of the other wheel. The main contribution of this thesis is the use of a single actuator with variable diameter wheels to drive and steer the base. A main advantage of the proposed concept design is the reduction in cost due to the use of a single actuator. One possible application for this design would be the Segway robot, where the steering would be controlled by shifting the driver's weight from side to another.

In addition to introducing the concept design for the proposed robot, we will also present the modeling, kinetostatic and dynamic analysis, which will enable us to derive the equations of motion of the robot. These results will be used to study the motion planning problem of the robot and explore both its abilities and limitations.

All these results and analysis will enable us eventually to gain a better understanding of the robot's properties and characteristics, and determine its practicality and usability.

## 1.6 Thesis Outline

This thesis is organized as follows. The model design is introduced in Chapter 2, where we will present a detailed description of the robot's parts and operation mechanism. In Chapter 3, the kinetostatic analysis is presented, where according to the obtained results, we will be able to simplify our model. The simplified model will be used in Chapter 4 where we will present the dynamic analysis and its corresponding simulation results to obtain the equations of motion. The derived equations of motion will be used in Chapter 5 to study the motion planning problem of the robot by applying Dubins curve to obtain the shortest path between two points. Finally, Chapter 6 provides some concluding remarks and future work.

# Chapter 2

## Model Design

The main purpose of this thesis is to design a differentially-driven robot with one actuator. In order to achieve this goal, variable-diameter wheels are used for the steering mechanism. The wheels are connected to the same drive shaft and therefore they have the same angular velocity. Hence, as one wheel decreases in diameter and the other increases, the robot steers in the direction of the wheel with the smaller diameter. The variation of the diameter of the wheels depends on the distribution of the weight of the drive mechanism. This drive mechanism acts as a pendulum that can rotate about the drive shaft and it can also be shifted along its length to either side by using two electromagnetic clutches that are powered by the same drive motor. The method of changing the wheels diameters is a passive control mechanism because the diameters are not directly controlled by the motor. There are two advantages for using a passive mechanism as compared to an active one. First, it is simpler than the latter where gears and drive shafts are used to change the wheels diameters. Second, it offers the possibility of substituting the moving mass by another one. For instance, in the case of a Segway, one can substitute the weight of the pendulum by that of a person. A schematic of the model design is shown in Fig. 2.1.

### 2.1 Model parts

The main parts of the robot are:

1. Shaft: the shaft is a pinion wire (*i.e.*, a very long spur gear) connected at its ends to the wheels and driven by the motor through a spur gear.
2. Frame: the frame is connected to the shaft by two bearings at an equal distance from both ends, and it acts as the main support for the carriage.
3. Carriage: the carriage is the main support for the actuator (or motor) and the clutches. It can slide along the frame when one of the clutches is activated.



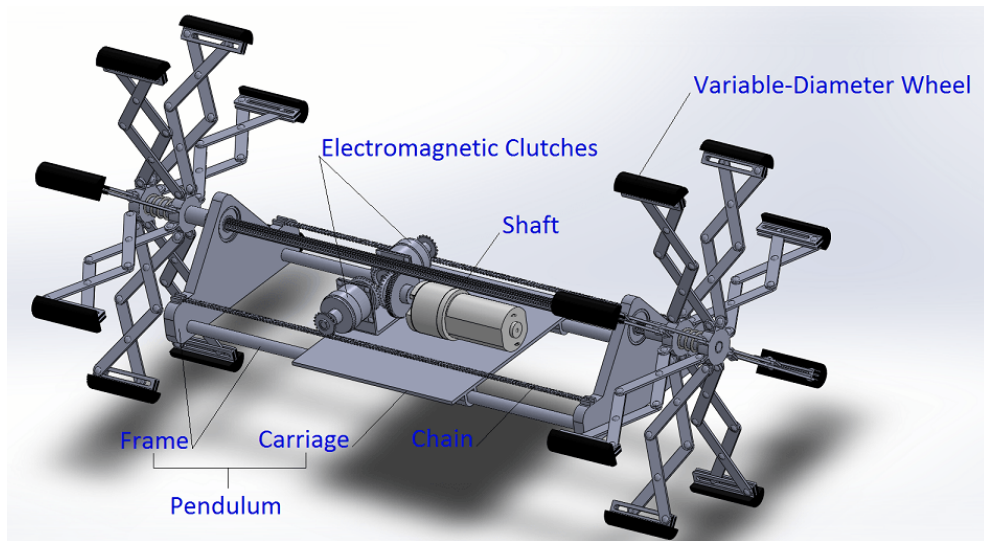


Figure 2.1: A mechanical design schematic of the proposed novel robotic platform.

4. Pendulum: the pendulum is a combination of the frame and carriage. It can rotate around the shaft and the position of its center of mass is affected by the position of the carriage on the frame.
5. Electric Motor: a simple DC motor which is the only actuator in the system. The motor is mounted by two gears, a spur gear connected to the shaft and a bevel gear connected to both clutches as shown in Fig. 2.2.
6. Electromagnetic Clutch: the clutch's main function is to connect its input shaft to its output shaft when activated. The input shaft is mounted by a bevel gear driven by the motor, while the output shaft is mounted by a sprocket connected to a chain fixed on the frame. When the clutch is activated, the output shaft will turn in one direction, causing the carriage to slide along the frame, thus shifting the robot's center of mass. Each clutch is used to move the carriage in a different direction. The clutches are not connected to each other and they cannot be activated at the same time.
7. Variable-Diameter Wheel: the wheel is mainly composed of four parts as shown in Fig. 2.3:
  - The two wheel rings which are mounted on the shaft where one is fixed at the edge of the shaft and the other can move freely along the shaft axis.
  - The scissor shaped rods which are attached at their base to the two rings. Their main function is to convert horizontal motion to verti-

cal motion or vice versa, which in return will cause a change in the diameters of the wheels.

- The wheel foot which acts as the contact point between the wheel and the ground.
- The coil spring which is mounted around the shaft and is attached at both ends to the two rings. When a force is applied to the spring, it will either elongate or compress according to its direction, thus, leading to a decrease or an increase in the wheel's diameter.

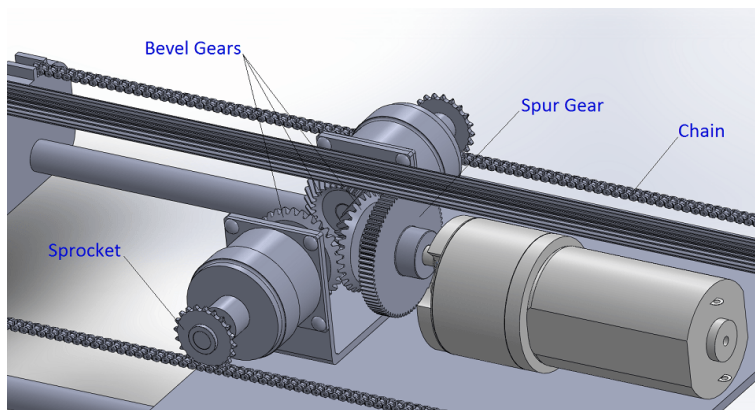


Figure 2.2: A detailed view of the transmission system.

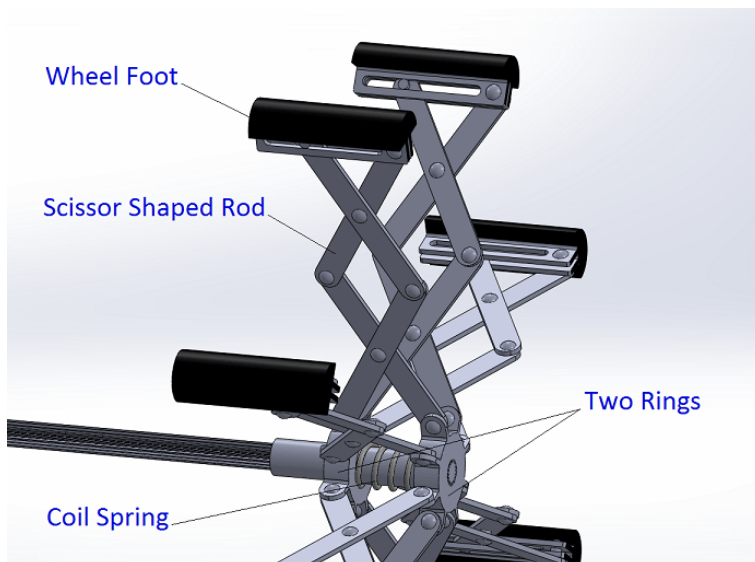


Figure 2.3: A detailed view of the wheel.

## 2.2 The operating mechanism

The main drive force of the robot is its pendulum. The motor is a part of the pendulum and is connected to the shaft by a spur gear. When the motor starts running, the pendulum will start rotating around the shaft until it reaches a certain height (*i.e.*, an equilibrium point) where the torque of the motor is equal to the torque induced by the weight of the pendulum. At this point, the wheels will start rotating and the pendulum will start falling back until it reaches another equilibrium point, hence the process starts all over again as shown in Fig 2.4.

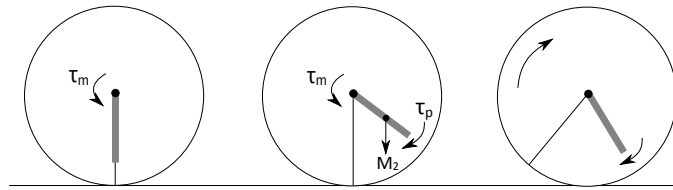


Figure 2.4: The pendulum drive mechanism.

In order to steer, one clutch is activated, thus connecting the input shaft of the clutch to its output shaft, which in turn will cause the power to be transferred from the motor through its bevel gear to the sprocket connected at the output shaft of the clutch. When the sprocket rotates, it will cause the carriage to move to one side, hence decreasing the wheel's diameter.

An overview of the whole system is presented in the Fig. 2.5.

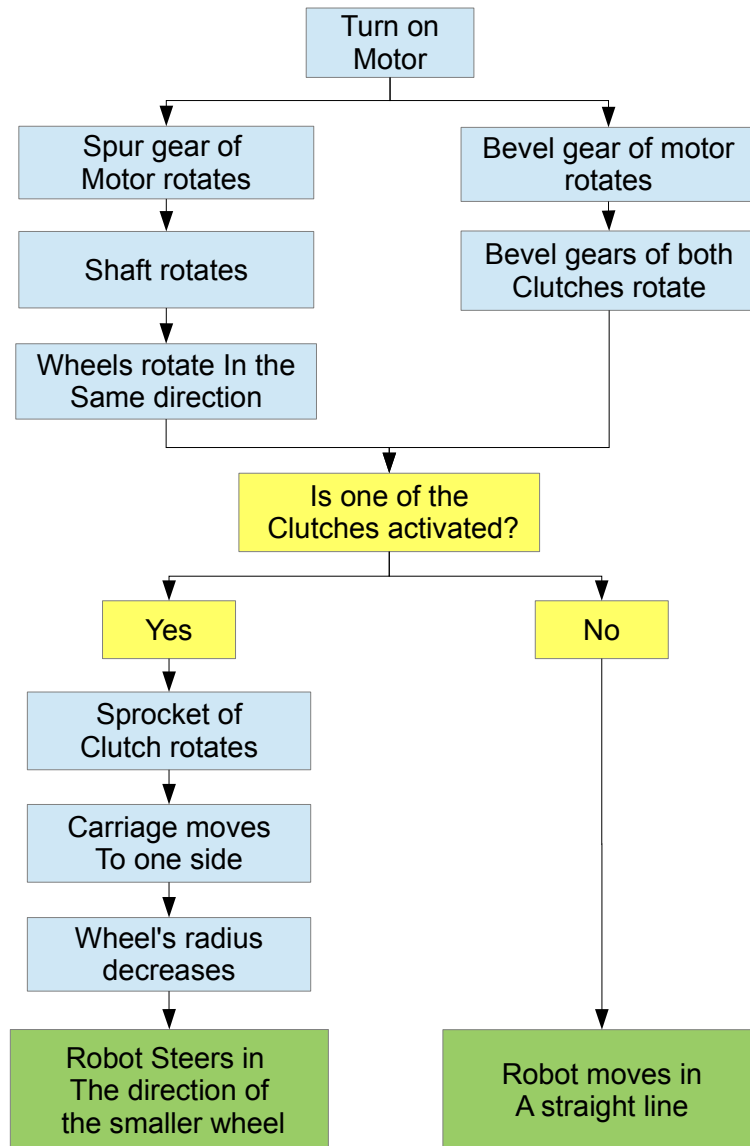


Figure 2.5: A flow chart describing the method of operation of the robot.

# Chapter 3

## Kinetostatic Analysis

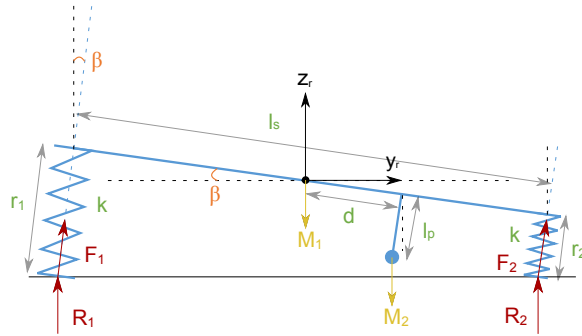
In this chapter we give an overview about the kinetostatic modelling followed by simulation results and analysis.

### 3.1 Kinetostatic Model

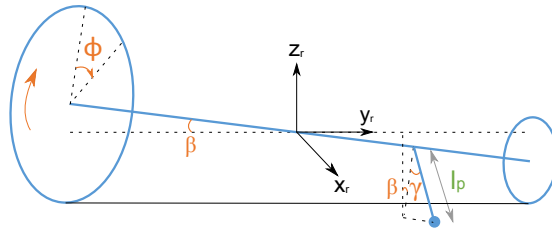
The kinetostatic model of the robot, as shown in Fig. 3.1, consists of two variable-diameter wheels modeled as two springs that are connected together by a central shaft. The shaft is mounted by a pendulum which can move along its length when one of the clutches is activated, thus, leading to a shift in the center of mass, which causes the variation in the diameters of the wheels. The system has two centers of mass where the first mass  $M_1$  represents the shaft with both wheels and is located at the center of the shaft, while the second mass  $M_2$  represents the pendulum and is located at distance  $l_p$  along the pendulum's axis. The radii of the wheels are represented by  $r_1$  and  $r_2$  respectively. The length of the shaft is denoted by  $l_s$ , the angle  $\beta$  represents its inclination from the horizontal and  $d$  is the distance of the pendulum from the shaft's center. The reaction forces on both wheels are represented by  $R_1$  and  $R_2$  respectively, while  $F_1$  and  $F_2$  represent the forces acting along the direction of the wheels.

It is also important to note, that in our analysis, we consider that the shape of the wheel is circular with a perimeter equal to the perimeter of the spoked wheel presented in Chapter 2. Therefore, the effects of the vibrations caused by the spoked wheel's shape are not taken into consideration, and hence will be studied as part of our future work along with other modifications and optimization in order to improve the proposed concept design.

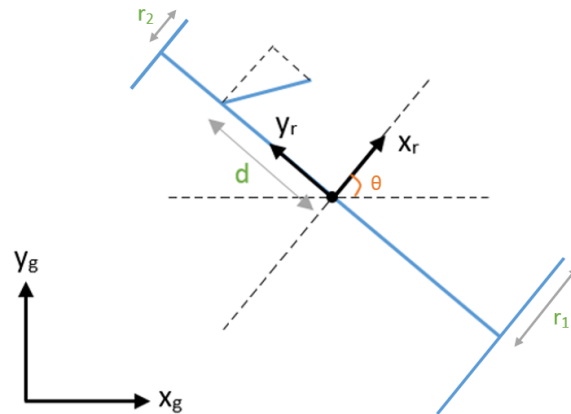
The system has two inputs. The first input is the angle of the motor  $|\alpha| = |\gamma| + |\phi|$  where  $\gamma$  represents the angle between the pendulum and the vertical axis  $-z_r$  and  $\phi$  is the angular rotation of the shaft or wheels as shown in Figure 3.1b, and the



(a) A front view of the model showing the forces and centers of mass.



(b) An isometric view of the model showing the angles  $\gamma$  and  $\phi$ .



(c) A top view of the model showing angle  $\theta$ .

Figure 3.1: The kinetostatic Model.

second input is the position of the pendulum  $d$  along the shaft. In order to control the steering angle  $\theta$  shown in Figure 3.1c, a relation between  $(d, \gamma)$  and  $(r_1, r_2)$  must be established, thus leading to a relation between  $(\theta)$  and  $(d, \gamma)$ . To

establish the preceding relation, a system of five equations is set to be solved:

$$\tan(\beta) = \frac{r_1 - r_2}{l_s} \quad (3.1)$$

$$r_0 - r_1 = \frac{R_1 \cos(\beta)}{k} \quad (3.2)$$

$$r_0 - r_2 = \frac{R_2 \cos(\beta)}{k} \quad (3.3)$$

$$R_1 + R_2 - M_1 g - M_2 g = 0 \quad (3.4)$$

$$\begin{aligned} -M_1 g(r_1 \sin(\beta) + \frac{l_s}{2} \cos(\beta)) - M_2 g(r_1 \sin(\beta) + (\frac{l_s}{2} + d) \cos(\beta) \\ - l_p \cos(\gamma) \sin(\beta)) + R_2(r_1 \sin(\beta) + l_s \cos(\beta) - r_2 \sin(\beta)) = 0 \end{aligned} \quad (3.5)$$

where  $r_0$  represents the radius of the wheels when no load is applied (*i.e.*,  $M_1 = M_2 = 0$ ),  $k$  is the stiffness of the spring,  $M_1$  is the mass of the wheels and shaft and  $M_2$  is the mass of the pendulum. Note that the first three equations are derived from geometry while the last two are derived from static equilibrium. The resultant  $r_1$  and  $r_2$  are both functions of  $(M_1, M_2, l_s, l_p, k, r_0, d, \gamma)$ . For a specific robot, the parameters  $(M_1, M_2, l_s, l_p, k, r_0)$  are all predefined constants, therefore,  $r_1$  and  $r_2$  can be solved for as functions of  $(d, \gamma)$  only, *i.e.*,  $r_1 = r_1(d, \gamma)$  and  $r_2 = r_2(d, \gamma)$ .

## 3.2 Simulations and Results

In order to study the effect of both  $(d, \gamma)$  on  $r_1$  and  $r_2$ , a set of simulations are carried out with the parameters values shown in Table 3.1. These values are chosen based on initial estimations made in the proposed design for the dimensions and masses of the robot's components. The results of four different simulations are presented below and the conclusions drawn are given thereafter.

Our first point of interest is to study the effect of  $d$  on  $r_1$  and  $r_2$  with  $\gamma = 0$ . As we can see from Fig. 3.2,  $r_1$  and  $r_2$  vary linearly as  $d$  is varied from  $-0.3\text{m}$  to  $0.3\text{m}$ .

The motivation for the second simulation is to investigate the effect of  $\gamma$  on  $r_1$  and  $r_2$  for different values of  $d$ . We vary  $\gamma$  between  $-\pi/2$  to  $\pi/2$  radians, while  $d$  is varied between  $-0.3\text{m}$  to  $0.3\text{m}$  with an increment of  $0.1\text{m}$ . Fig. 3.3 presents the results for this simulation applied only on  $r_1$  (same behavior will be obtained for  $r_2$  due to the symmetry of the system). One can notice that as  $\gamma$  deviates from 0,  $r_1$  slightly increases. Increasing the value of  $d$  causes larger variations of

Table 3.1: Simulation Parameters.

Parameter	Value
$M_1$	2 kg
$M_2$	2 kg
$l_s$	0.6 m
$k$	250 N/m
$r_0$	0.15 m
$l_p$	0.07 m

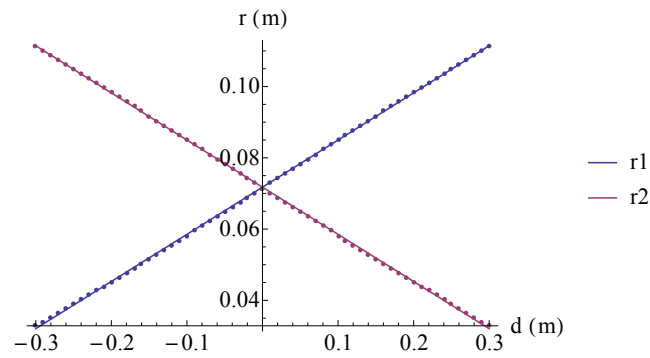


Figure 3.2: The effect of variation of  $d$  on  $r_1$  and  $r_2$  with  $\gamma = 0$ .

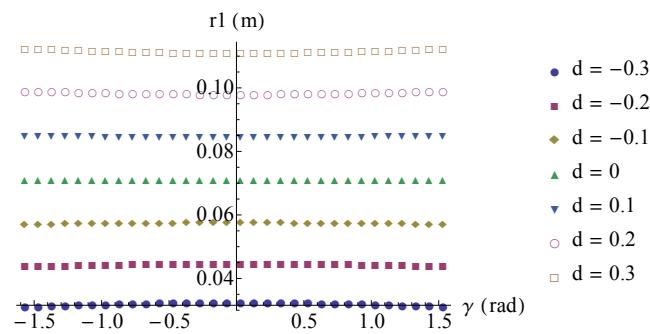


Figure 3.3: The effect of  $\gamma$  on  $r_1$  for different values of  $d$ .

$r_1$  for the same  $\gamma$ . However, these variations are very small and can be neglected.



In order to better perceive the effect of  $\gamma$ , another simulation is conducted using only one value of  $d = -0.3\text{m}$  as shown in Fig. 3.4. Here we can notice that the value of  $r_2$  varies between  $0.1115\text{ m}$  to  $0.1129\text{ m}$ , which consists of only  $1.2\%$  variation, thus it is justifiable to consider the effect of  $\gamma$  on  $r_1$  and  $r_2$  as negligible.

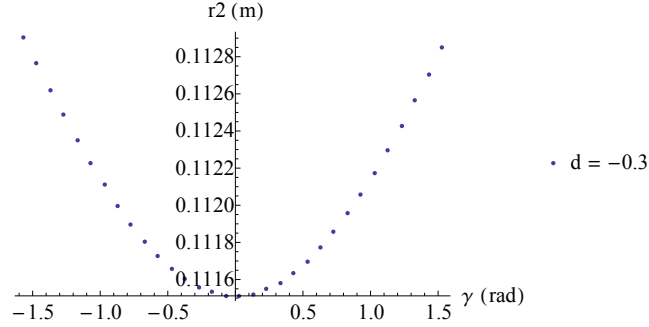


Figure 3.4: The effect of  $\gamma$  on  $r_2$  for  $d = -0.3\text{m}$ .

Finally, in Fig. 3.5, we analyze the effect of  $\gamma$  and  $d$  on the height of the center of mass  $M_2$  (*i.e.*, the height of the center of the shaft).  $\gamma$  is varied between  $-\pi/2$  to  $\pi/2$  radians, and  $d$  is varied between  $-0.3\text{m}$  to  $0.3\text{m}$ . We notice that the height varies between  $0.07152\text{ m}$  and  $0.071575\text{ m}$ , thus changing only by  $0.08\%$  and rendering the effect negligible. Moreover, we can notice that the curves overlap for the same absolute value of  $|d|$  due to the symmetry of the system.

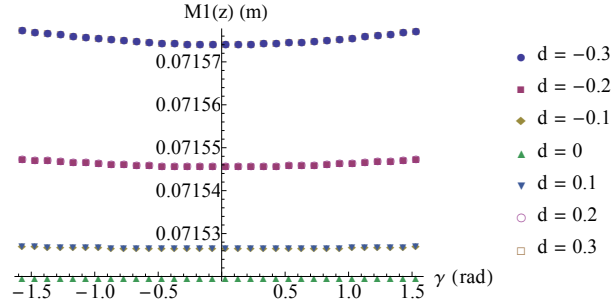


Figure 3.5: The effect of  $\gamma$  and  $d$  on the height of the center of mass  $M_1$ .

Based on the results obtained from these simulations, the following conclusions can be drawn:

1. The effect of  $\gamma$  on the variation of  $r_1$  and  $r_2$  is negligible, thus  $r_1$  and  $r_2$  are considered as functions of  $d$  only. Moreover, based on Simulation 1 shown in Fig. 3.2, we conclude that the relation between  $r_1$ ,  $r_2$  and  $d$  is linear. Hence, the resulting equations are:

$$r_1 = c_1 d + c_2$$

$$r_2 = -c_1 d + c_2$$

To calculate  $c_1$  and  $c_2$ , we apply Hooke's Law.

For  $c_2$ , the pendulum is at the center of the shaft where  $d = 0$ , so the centers of mass of  $M_1$  and  $M_2$  are located at the center, hence the applied force on both wheels is equal and has a value of  $\frac{M_1 g + M_2 g}{2}$ . Therefore  $c_2$  is equal to:

$$c_2 = r_0 - \frac{M_1 g + M_2 g}{2k}$$

Regarding  $c_1$ , the pendulum will be located at  $d_{max} = \frac{l_s}{2}$ , hence the weight of the pendulum will be supported by only one wheel. Therefore  $c_1$  is equal to:

$$c_1 = r_0 - \frac{(\frac{M_1 g}{2} + M_2 g) \cos(\beta)}{k}$$

2. Based on Fig. 3.5, we can deduce that the height of the center of mass  $M_2$  is almost constant and has a value equal to:

$$r = \frac{r_1 + r_2}{2}$$

3. Since  $\gamma$  has no effect on  $r_1$  and  $r_2$ , we can also conclude that  $\gamma$  has no effect on the steering angle  $\theta$  (*i.e.*,  $\theta$  is independent of  $\gamma$ ). Therefore,  $\theta$  can be calculated in the following way for fixed values of  $r_1$  and  $r_2$  (*i.e.*, constant value of  $d$ ):

$$R = \frac{l_s v_1 + v_2}{2 v_1 - v_2} = \frac{l_s r_1 + r_2}{2 r_1 - r_2} = \frac{l_s c_2}{2 c_1 d}$$

$$S = \frac{\phi(t)(r_1 + r_2)}{2}$$

where  $R$  is the radius of curvature and  $S$  is the distance traveled by the robot as shown in Fig. 3.6.

Thus,  $\theta(t)$  is equal to:

$$\theta(t) = \frac{S}{R} = \frac{\phi(t)(r_1 - r_2)}{l_s} = c_1 d \phi(t)$$

and  $\dot{\theta}(t)$  will be equal to:

$$\dot{\theta}(t) = c_1 d \dot{\phi}(t)$$

Therefore, to calculate  $\theta(t)$  for any moment in time with variable values of  $d(t)$  and  $\phi(t)$ , we have:

$$\theta(t) = \int_0^t c_1 d(t) \dot{\phi}(t) dt$$

Finally, based on these conclusions, we can simplify the system and model it as a vertical rolling disk having a constant radius  $r = \frac{r_1 + r_2}{2}$  with a pendulum attached to its center and acting as the driving force.

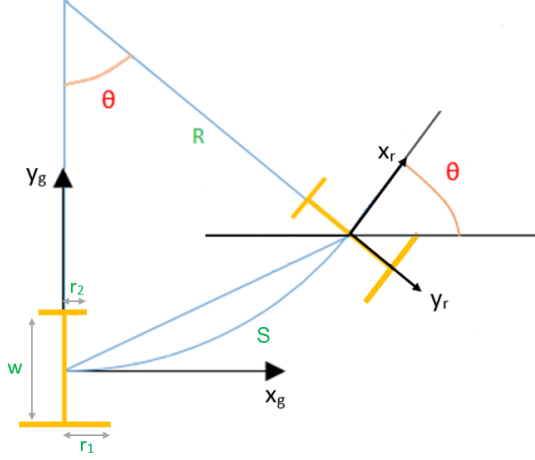


Figure 3.6: The trajectory followed by the robot for a constant value of  $d$ .

### 3.3 Parameters Analysis

The previous conclusions were derived according to the design parameters specified in table 3.1. But changing these parameters can alter the behavior of the system and render these conclusions invalid. Therefore, we perform some parameters analysis to study the effects of changing these parameters.

Our main concern is to study the effect of  $\gamma$  on  $r_1$ ,  $r_2$  and the height of center of mass  $M_1$ .

The first parameter to be studied is the ratio  $\frac{M_1}{M_2}$ . This ratio represents the distribution of the total mass between the pendulum and the body. When the pendulum is shifted to either side of the robot, if the proportion of its mass is larger than that of the body, the center of mass of the robot will shift towards the pendulum's direction. Hence, the force applied to the wheel on that side will be greater, and thus the radius of the wheel will decrease.

In Simulation 1 shown in Fig. 3.7, we study the effect of changing  $\gamma$  on  $r_1$  for different values of  $\frac{M_1}{M_2}$  at  $d = -0.3$ . We can notice two things happening as the ratio  $\frac{M_1}{M_2}$  decreases (*i.e.*, the weight of the pendulum increases while the weight of the body decreases). First, the average value of the wheel's radius will decrease, and that's because the center of mass of the robot is shifted towards the pendulum's direction. And secondly, the effect of changing  $\gamma$  on  $r_1$  increases and reaches about 2mm for  $\frac{M_1}{M_2} = \frac{1}{3}$ . Therefore, we can conclude that having small values of the ratio  $\frac{M_1}{M_2}$  can have a considerable effect on the wheel's radius.

In Simulation 2 shown in Fig 3.8, we study the effect of changing  $\gamma$  on  $M_1(z)$  for different values of  $\frac{M_1}{M_2}$  at  $d = -0.3$ . We can also notice two things happening as the ratio  $\frac{M_1}{M_2}$  decreases. First, the average value of  $M_1(z)$  slightly increases, and secondly, the effect of changing  $\gamma$  on  $M_1(z)$  increases. But these effects are very

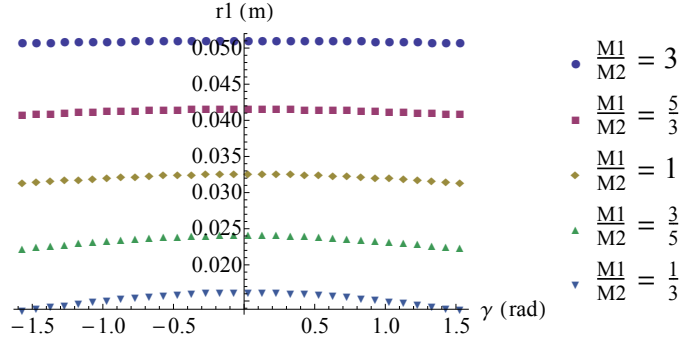


Figure 3.7: Simulation 1: The effect of changing  $\gamma$  on  $r_1$  for different values of  $\frac{M_1}{M_2}$  at  $d = -0.3$ .

small and hence can be considered negligible.

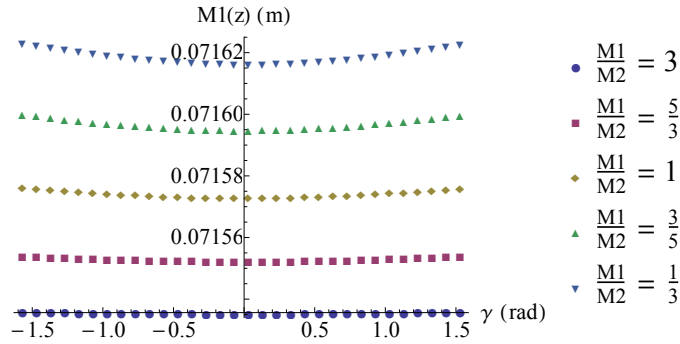


Figure 3.8: Simulation 2: The effect of changing  $\gamma$  on  $M_1(z)$  for different values of  $\frac{M_1}{M_2}$  at  $d = -0.3$ .

The second parameter to be studied is the ratio  $\frac{l_s}{r_0}$ . We have noticed previously from Fig. 3.3 and Fig. 3.5 that by increasing  $d$ , the effect of changing  $\gamma$  also increases. But in this section, we aim to study the effects of changing the length of the shaft, for a constant value of  $d$ , while changing  $\gamma$ .

In Simulation 3 shown in Fig. 3.9, we study the effect of changing  $\gamma$  on  $r_1$  for different values of  $\frac{l_s}{r_0}$  at  $d = -0.3$ . We can notice two things happening as the ratio  $\frac{l_s}{r_0}$  increases. First, the average value of the wheel's radius will increase, and that's because the center of mass of the robot is shifted towards the shaft's center. And secondly, the effect of changing  $\gamma$  on  $r_1$  decreases from 2mm at  $\frac{l_s}{r_0} = 4$  to about 0mm at  $\frac{l_s}{r_0} = 8$ . Therefore, we can conclude that changing the shaft's length can have a considerable effect on the wheel's radius.

In Simulation 4 shown in Fig. 3.10, we study the effect of changing  $\gamma$  on  $M_1(z)$  for different values of  $\frac{l_s}{r_0}$  at  $d = -0.3$ . We can notice that both effects of increasing the ratio  $\frac{l_s}{r_0}$  and changing  $\gamma$  are very small, and thus can be considered negligible.

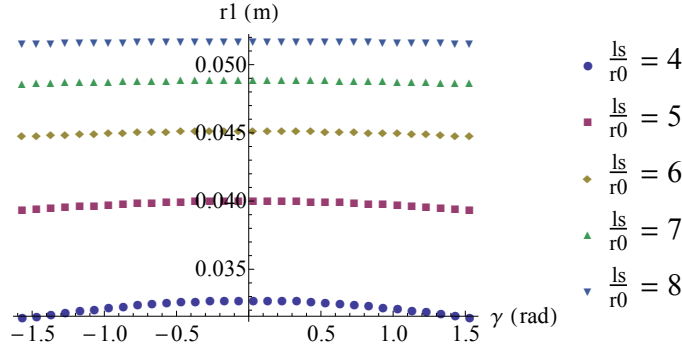


Figure 3.9: Simulation 3: The effect of changing  $\gamma$  on  $r_1$  for different values of  $\frac{l_s}{r_0}$  at  $d = -0.3$ .

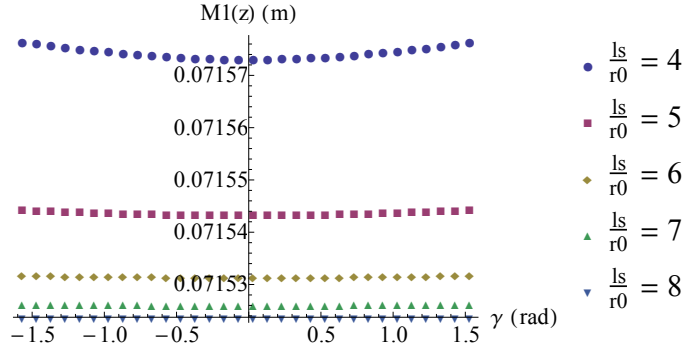


Figure 3.10: Simulation 4: The effect of changing  $\gamma$  on  $M_1(z)$  for different values of  $\frac{l_s}{r_0}$  at  $d = -0.3$ .

The third and final parameter to be studied is the ratio  $\frac{l_p}{r_0}$ . Here we will study the effects of changing the length of the pendulum on  $r_1$  and  $M_1(z)$  while changing  $\gamma$ . This parameter was chosen because by changing the pendulum's length, its center of mass will change, hence shifting the whole robot's center of mass.

In Simulation 5 shown in Fig. 3.11, we study the effect of changing  $\gamma$  on  $r_1$  for different values of  $\frac{l_p}{r_0}$  at  $d = -0.3$ . The results obtained are interesting. We can notice that for  $\gamma = 0$ , the wheel's radius increases by about 1mm as  $\frac{l_p}{r_0}$  increases. This is due to the fact that as the length of the pendulum is increased, its center of mass is shifted towards its edge, and because the shaft will be tilted by an angle  $\beta$  as shown in Fig. 3.1a, the center of mass of the pendulum will be closer to the center of the robot, thus decreasing the weight applied on the wheel. However, when  $\gamma = \frac{\pi}{2}$  or  $\gamma = \frac{-\pi}{2}$ , the pendulum will be in a horizontal position, hence its center of mass will be at an equal distance from the shaft's center for all values of  $l_p$ , therefore, the value of  $r_1$  will stay constant. Based on these observations,

we can conclude that changing the pendulum's length can have a considerable effect on the wheel's radius.

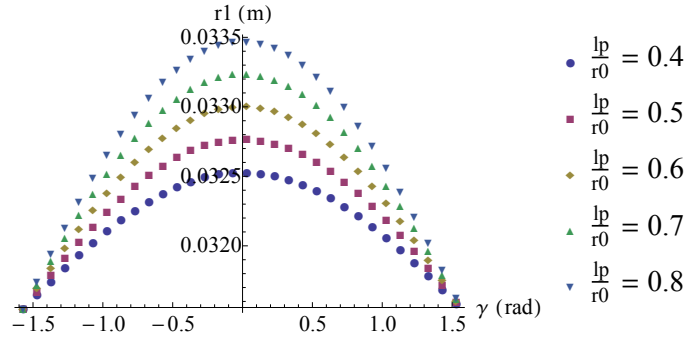


Figure 3.11: Simulation 5: The effect of changing  $\gamma$  on  $r_1$  for different values of  $\frac{l_p}{r_0}$  at  $d = -0.3$ .

Finally, in Simulation 6 shown in Fig. 3.12, we study the effect of changing  $\gamma$  on  $M_1(z)$  for different values of  $\frac{l_p}{r_0}$  at  $d = -0.3$ . The results obtained are similar in behavior to simulation 5, but the differences in values are very small and thus can be considered negligible.

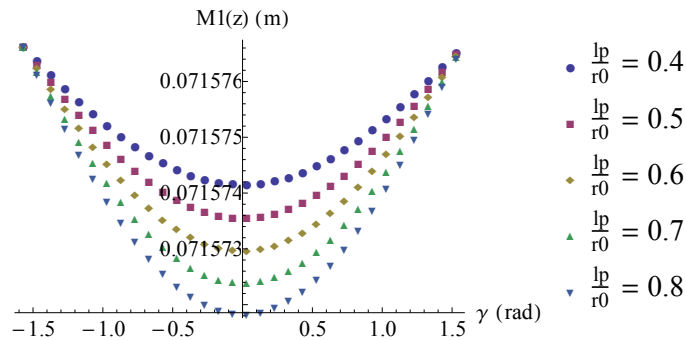


Figure 3.12: Simulation 6: The effect of changing  $\gamma$  on  $M_1(z)$  for different values of  $\frac{l_p}{r_0}$  at  $d = -0.3$ .

# Chapter 4

## Dynamic Analysis

In this chapter, we present the dynamic analysis of the robot followed by simulation results.

### 4.1 Dynamic Model

As a result of the conclusions drawn from the kinetostatic analysis, we model the robot as a vertical rolling disk with a pendulum, with  $M_1$  being the center of mass of the rolling disk of radius  $r$  and  $M_2$  the center of mass of the pendulum of length  $l_p$  as shown in Fig. 4.1. In addition,  $\theta$  is the steering angle of the disk around  $z_r$ ,  $\phi$  is the angular distance travelled by the disk measured with respect to the  $z_r$  axis, and  $\gamma$  is the angle of the pendulum measured with respect to the  $-z_r$  axis on the disk.

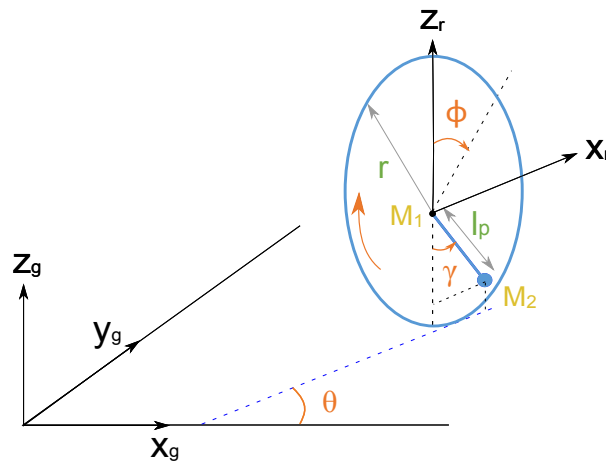


Figure 4.1: The dynamic Model.

One of the adopted methods for deriving the equations of motion is the La-

grangian mechanics theorem. This method is a reformulation of classical mechanics and is mathematically equivalent to the Newtonian approach. It is based on examining the kinetic and potential energies of a system of objects and the equations of motion are derived by computing the Euler-Lagrange equations. We adopt this approach for our design because of the advantage given by the minimum number of generalized coordinates that can be chosen by convenience to exploit symmetries in the system and the ease of incorporating the nonholonomic constraint forces that are acting on the system. The Lagrangian steps are given as follows:

1. Defining the generalized coordinates:

$$q = \begin{bmatrix} x \\ y \\ \phi \\ \alpha \end{bmatrix}$$

with  $\theta(t) = \int_0^t c_1 d(t) \dot{\phi}(t) dt$ . Note that, for our system, only the steering angle  $\theta$  and the pendulum angle  $\alpha$  are actuated degrees of freedom.

2. Finding the locations of centers of mass:

$$p_1 = \begin{bmatrix} x \\ y \\ r \end{bmatrix}$$

$$p_2 = \begin{bmatrix} x + l_p \sin(\alpha + \phi) \cos \theta \\ y + l_p \sin(\alpha + \phi) \sin \theta \\ r - l_p \cos(\alpha + \phi) \end{bmatrix}$$

where  $\gamma = \alpha + \phi$  (since  $\phi$  is negative).

3. Deriving the velocities of the centers of mass:

$$\begin{bmatrix} v_1 \\ v_2 \end{bmatrix} = \begin{bmatrix} \dot{p}_1 \\ \dot{p}_2 \end{bmatrix}$$

4. Finding the constraints direction:

$$k_1 = \begin{bmatrix} \cos(\theta - \frac{\pi}{2}) \\ \sin(\theta - \frac{\pi}{2}) \\ 0 \end{bmatrix}$$

$$k_2 = \begin{bmatrix} \cos \theta \\ \sin \theta \\ 0 \end{bmatrix}$$



5. Expressing the nonholonomic constraints kinematically:

$$C_1 = k_1.v_1 = \dot{x} \sin \theta - \dot{y} \cos \theta = 0$$

$$C_2 = k_2.v_2 - r\dot{\phi} = \dot{x} \cos \theta + \dot{y} \sin \theta - r\dot{\phi} = 0$$

$$\begin{bmatrix} C_1 \\ C_2 \end{bmatrix} = m.\dot{q} = 0$$

$$m = \begin{bmatrix} \sin \theta & -\cos \theta & 0 & 0 \\ \cos \theta & \sin \theta & -r & 0 \end{bmatrix}$$

6. Calculating the constraints forces in terms of the Lagrange multipliers,  $\lambda_1$  and  $\lambda_2$ :

$$f_c = m^t. \begin{bmatrix} \lambda_1 \\ \lambda_2 \end{bmatrix} = \begin{bmatrix} \lambda_1 \sin \theta + \lambda_2 \cos \theta \\ -\lambda_1 \cos \theta + \lambda_2 \sin \theta \\ -r\lambda_2 \\ 0 \end{bmatrix}$$

7. Evaluating the generalized forces vector:

$$\tau = [0 \quad 0 \quad 0 \quad \tau_\alpha]$$

The value of  $\tau_\alpha$  is calculated by controlling the value of  $\alpha$  using the inverse dynamics controller.

$$\tau_\alpha = \ddot{\alpha}_d + 2w(\dot{\alpha}_d - \dot{\alpha}) + w^2(\alpha_d - \alpha)$$

with  $\alpha_d$  being the desired angle  $\alpha$ .

8. Calculating the potential energy:

$$PE = M_1gp_{1z} + M_2gp_{2z}$$

9. Calculating the kinetic energy:

$$KE = \frac{1}{2}M_1(v_1^2) + \frac{1}{2}M_2(v_2^2) + \frac{1}{2}J_1(\dot{\theta}^2) + \frac{1}{2}J_2(\dot{\phi}^2) + \frac{1}{2}J_3(\dot{\alpha}^2)$$

where  $J_1$  and  $J_2$  are the moments of inertia of the disk around  $\theta$  and  $\phi$  respectively, and  $J_3$  is the moment of inertia of the pendulum around  $\alpha$ . It is also worthy to mention that the moment of inertia of the pendulum around  $\theta$  is not calculated since it has no effect on the robot's behavior due to two reasons. First, due to the fact that both wheels are attached to the same shaft and can only rotate in the same direction, and second, due to the nonholonomic constraints presented earlier, thus prohibiting any rotation around the  $z_r$  axis.

10. Calculating the Lagrangian:

$$L = KE - PE$$

11. Computing the Euler-Lagrange equations of motion

$$\frac{d}{dt} \frac{\partial L}{\partial \dot{q}_i} - \frac{\partial L}{\partial q_i} = \tau_i$$

for all  $i = 1, \dots, 4$ .

## 4.2 Simulations and Results

This section presents simulation results and analysis for the proposed dynamics model. The equations of motion are derived from the equations of section 4.1. The simulation parameters are the same as those given in Table 3.1.

For the first simulation shown in Fig. 4.2a, the initial conditions used are as follows:

$$\begin{aligned} x[0] = y[0] = \theta[0] = \phi[0] = 0, \quad \alpha[0] = \alpha_d[0] \\ \dot{x}[0] = \dot{y}[0] = \dot{\theta}[0] = \dot{\phi}[0] = \dot{\alpha}[0] = 0 \end{aligned}$$

With the following inputs:

$$d = 0.3, \quad \alpha_d = 0.1t$$

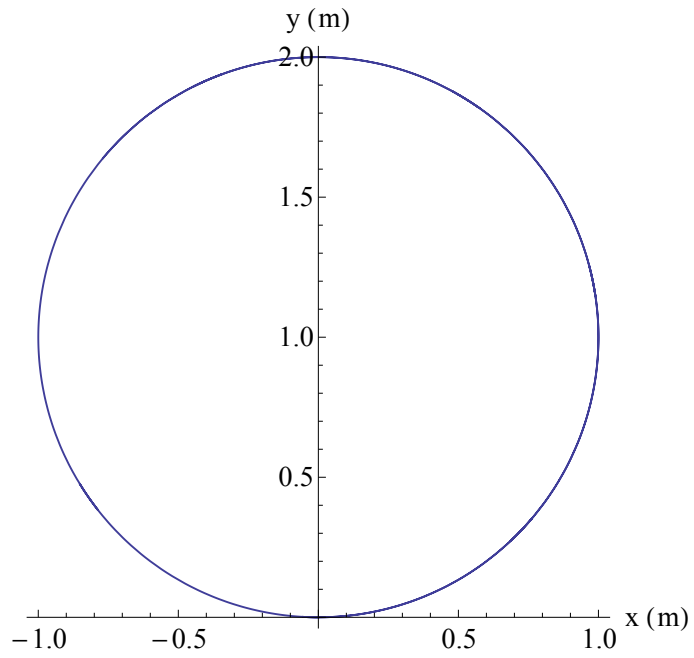
While for the second simulation shown in Fig. 4.2b, the initial conditions used are as follows:

$$\begin{aligned} x[0] = y[0] = \phi[0] = 0, \quad \theta[0] = \frac{\pi}{4}, \quad \alpha[0] = \alpha_d[0] \\ \dot{x}[0] = \dot{y}[0] = \dot{\theta}[0] = \dot{\phi}[0] = \dot{\alpha}[0] = 0 \end{aligned}$$

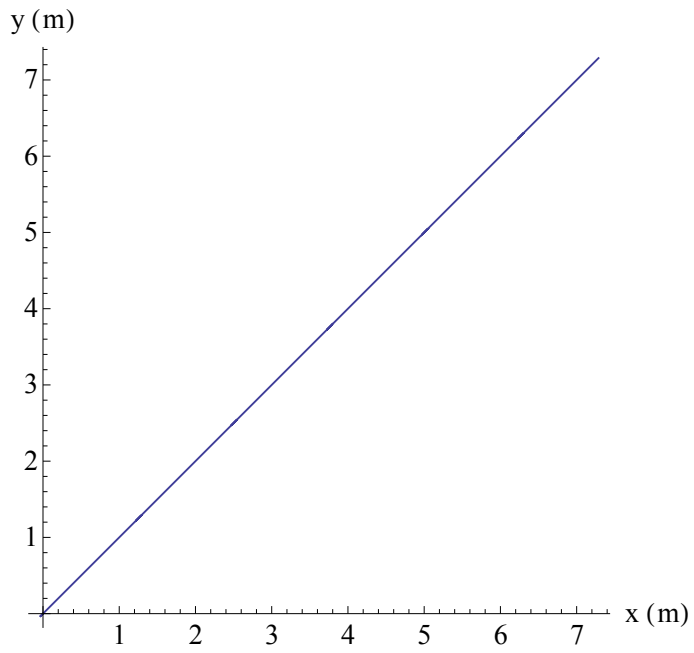
With the following inputs:

$$d = 0, \quad \alpha_d = 0.1t$$

The results of Fig. 4.2 show that the robot will turn in a perfect circle for a constant value of  $d$ , and will follow a straight line when  $d = 0$  as it is expected. The importance of these results is shown when studying the motion planning problem of the robot, where will we use Dubins Curve [22], which requires the use of maximum curvature and straight line segments to achieve the shortest path between two points.



(a) Simulation 1: A circular path traveled by the robot.



(b) Simulation 2: A straight line path traveled by the robot.

Figure 4.2: The trajectories of the robot for different initial conditions and values of  $d$ .

# Chapter 5

## Motion Planning

In this Section, we introduce a method for planning the motion of the robot. Given that the proposed platform is planar, a time optimal trajectory between two locations with specified orientations was specified in [22]. It was shown that between any two configurations, the shortest path in a 2D plane can always be expressed as a combination of no more than three motion primitives. Each motion primitive applies a constant action over an interval of time. Furthermore, the only actions that are needed to traverse the shortest paths are (S,L,R). The  $S$  primitive drives the car straight ahead. The  $L$  and  $R$  primitives turn as sharply as possible to the left and right, respectively. Using these symbols, each possible kind of shortest path can be designated as a sequence of three symbols that corresponds to the order in which the primitives are applied. Let such a sequence be called a *word*. There is no need to have two consecutive primitives of the same kind because they can be merged into one. Under this observation, ten possible words of length three are possible. Dubins showed that only these six words are possibly optimal: LRL, RLR, LSL, LSR, RSL and RSR. The shortest path between any two configurations can always be characterized by one of these words. These are called the Dubins curves. One example is shown in Fig. 5.1. The two main restrictions that make Dubins curves time optimal are: the robotic

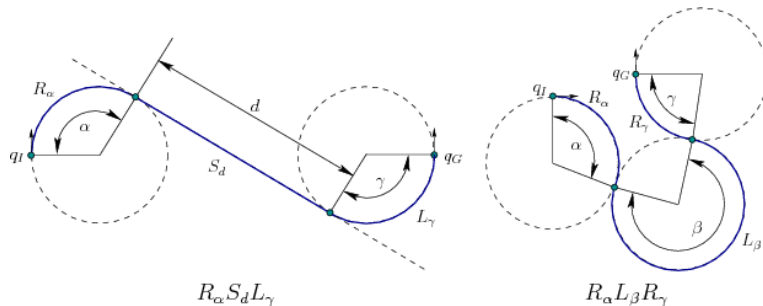


Figure 5.1: Two examples of Dubins curve: the first has a RSL configuration and the second has a RLR configuration.

platform must have constant speed and it must have a minimum turning radius. For systems with such restrictions, the time optimal curve, that is, the shortest curve connecting two points in a two dimensional plane is a path consisting of maximum curvature and/or straight line segments i.e., this path will be made by joining circular arcs of maximum curvature and straight lines [22].

For the proposed platform, there exists a maximum turning angle. This is due to the fact that none of the wheel diameters can shrink to zero diameter. Thus, a time optimal path would be a Dubins curve. For the proposed platform to traverse time optimal trajectories, the transition between arcs with opposite curvatures or arc and straight lines must happen in minimal time, that is,  $\dot{d}$  must be sufficiently large during the transition.

## 5.1 Perfect Dubins Curve

For our first attempt, we decided to obtain a perfect dubins curve in order to test the correctness of our system. In the first simulation shown in Fig. 5.2b, we move the robot from one point to another by giving it a set of open-loop commands to follow. In this particular example, the robot must first steer by  $\pi/4$  radians, then move in a straight line for 1m and finally steer again by  $-\pi/4$  radians. In order to achieve this, we use a step function for the input  $d(t)$  as shown in Fig 5.2a. The initial conditions used are:

$$x[0] = y[0] = \theta[0] = \phi[0] = 0, \quad \alpha[0] = \alpha_d[0]$$

$$\dot{x}[0] = \dot{y}[0] = \dot{\theta}[0] = \dot{\phi}[0] = \dot{\alpha}[0] = 0$$

with the second input  $\alpha_d$  equal to:

$$\alpha_d = 0.1t$$

and the maximum radius of curvature is determined by:

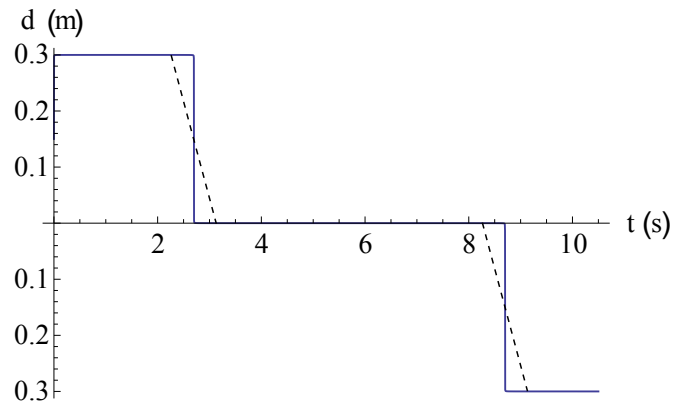
$$R_{max} = \frac{l_s}{2} \frac{c_2}{c_1 d_{max}}$$

with:

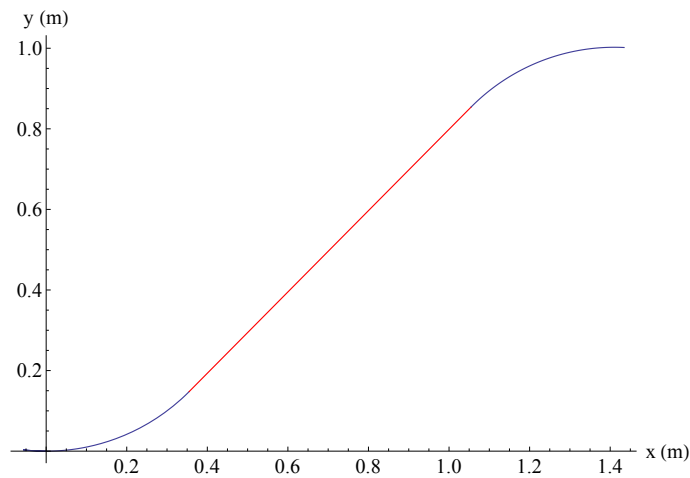
$$c_1 = r_0 - \frac{(\frac{M_1 g}{2} + M_2 g) \cos(\beta)}{k}$$

$$c_2 = r_0 - \frac{M_1 g + M_2 g}{2k}$$

We can notice from the result, that the final angle of rotation  $\theta$  is equal to 0 which indicates that the obtained path is a perfect Dubins curve. However, this was achieved using a step function for  $d(t)$ , which means that the transitions between



(a) The variation of  $d(t)$  as a step function.



(b) Simulation 3: An ideal Dubins curve trajectory traveled by the robot.

Figure 5.2: An ideal Dubins curve trajectory with the corresponding step function  $d(t)$ .

one constant value of  $d(t)$  to another is done instantaneously as shown in Fig. 5.2a. In realistic scenarios and according to our design presented in Chapter 2,  $d(t)$  cannot change instantaneously, and thus the transition from one value to another will be linear as shown by the dashed lines in Fig. 5.2a. These linear transitions will affect the robot's path, which implies that a perfect Dubins curve cannot be achieved.

## 5.2 Real Dubins Curve

In this section, we present the different steps needed to obtain a real dubins curve for our model followed by simulations results.

### 5.2.1 Calculating the Function $d(t)$

In order to obtain a real representation for our system's dubins curve, the function  $d(t)$  must include the transition phases represented by the dashed lines in Fig. 5.2a. To obtain the function  $d(t)$ , we must calculate the slope or the transition speed  $\dot{d}$  which is proportionally related to the angular velocity of the motor  $\dot{\alpha}$  by the following equation:

$$\dot{d} = \dot{\alpha} \frac{N_1}{N_2} \frac{d_{p3}}{2}$$

Where  $N_1$  and  $N_2$  are the number of teeth of gear 1 and gear 2 respectively, and  $d_{p3}$  is the pitch diameter of gear 3 as shown in Fig. 5.3.

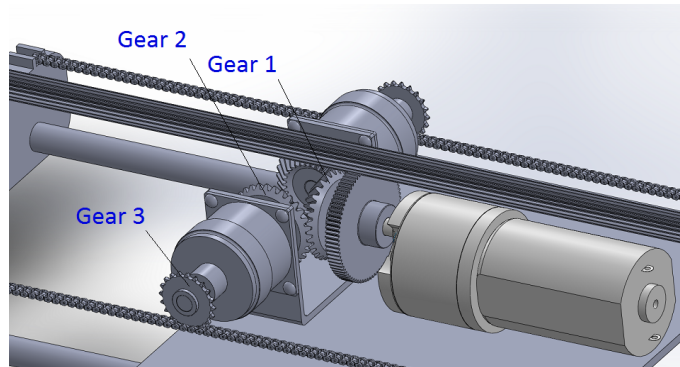


Figure 5.3: The transmission system showing the gears numbers.

If  $\dot{\alpha}$  is constant, than  $\dot{d}$  is constant and  $d(t)$  will act as a linear function during the transition phase as shown previously by the dashed lines in Fig. 5.2a.

### 5.2.2 Simplified Dynamic Model

In an attempt to obtain the real dubins curve using the new function of  $d(t)$ , we faced a mathematical problem for the calculation of  $\theta(t)$ . In our previous simulations,  $d(t)$  was considered as a constant parameter, and hence  $\theta(t)$  was calculated using the following equation:

$$\theta(t) = c_1 d \phi(t)$$

Whereas, in our new simulations,  $d(t)$  can no more be assumed to be a constant parameter, and hence  $\theta(t)$  is calculated as follows:

$$\theta(t) = \int_0^t c_1 d(t) \dot{\phi}(t) dt$$

However, no closed form of  $\theta(t)$  could be obtained and therefore, the system has no solution in that case.

Therefore, to solve the real dubins curve, we opted to simplify the dynamic model of our design. In the new model, we consider the rolling disk to be moving in only one dimension (x-direction). Hence, there is no angle of rotation  $\theta(t)$ , and the positions of the disk and pendulum are calculated using only angles  $\phi(t)$  and  $\alpha(t)$ . After applying the Lagrangian theorem to our new model, we use the obtained interpolating function of  $\phi(t)$  to calculate  $x(t)$ ,  $y(t)$  and  $\theta(t)$  kinematically.

In other words, in our new model, we're assuming that the dynamics forces will only affects the forward and backwards motion of our robot, and that the steering angle is not affected by any forces and thus can be calculated kinematically. However, this assumption is valid and will not affect any result, and this is due to the following three reasons:

1. The nonholonomic constraints used will prevent the wheels from slipping or skidding, thus any centrifugal force when steering will have no effect on the robot.
2. The wheels are attached to the same shaft, which means that they can only rotate in the same direction. Therefore, along with the nonholonomic constraints, it will prevent the moments of inertia of the pendulum and disk around  $z_r$  (z axis of the robot) to have any effect on the steering angle.
3. The obtained result of a perfect circular path in Fig. 4.2a proves that the dynamics forces have no effect on the steering angle or else the path wouldn't be a perfect circle.

The new Lagrangian steps are summarized as follows:

1. Defining the generalized coordinates:

$$q = \begin{bmatrix} \phi \\ \alpha \end{bmatrix}$$

2. Finding the locations of centers of mass:

$$p_1 = \begin{bmatrix} r\phi(t) \\ 0 \\ r \end{bmatrix}$$



$$p_2 = \begin{bmatrix} r\phi(t) + l_p \sin(-\phi(t) + \alpha(t)) \\ 0 \\ r - l_p \cos(-\phi(t) + \alpha(t)) \end{bmatrix}$$

3. Calculating the potential energy:

$$PE = M_1 g p_{1z} + M_2 g p_{2z}$$

4. Calculating the kinetic energy:

$$KE = \frac{1}{2} M_1 (v_1^2) + \frac{1}{2} M_2 (v_2^2) + \frac{1}{2} J_2 (\dot{\phi}^2) + \frac{1}{2} J_3 (\dot{\alpha} + \dot{\phi})^2$$

5. Calculating the Lagrangian:

$$L = KE - PE$$

with the other remaining steps being the same as the original model.

After deriving the equations of motion and obtaining the interpolating functions of  $\phi(t)$  and  $\dot{\phi}(t)$ , we then calculate  $\theta(t)$  numerically with the following equation:

$$\theta(t) = \int_0^t c_1 d(t) \dot{\phi}(t) dt$$

And finally we calculate  $x(t)$  and  $y(t)$  as follows:

$$x(t) = \int_0^t \frac{r}{2} \dot{\phi}(t) \cos \theta(t) dt$$

$$y(t) = \int_0^t \frac{r}{2} \dot{\phi}(t) \sin \theta(t) dt$$

### 5.2.3 Simulations and Results

In this section we present the simulations results for the simplified dynamic model and examine the difference between the real and perfect dubins curves.

The simulation parameters used are the same as those given in Table 3.1.

For the first simulation shown in Fig. 5.5, the set of commands used for the open-loop dubins curve is:

1. Turn by  $\frac{\pi}{8}$  rad
2. Move in straight line for 0.5m

3. Turn by  $-\frac{\pi}{8}\text{rad}$

The initial conditions used are as follows:

$$x[0] = y[0] = \theta[0] = \phi[0] = 0, \alpha[0] = \alpha_d[0]$$

$$\dot{x}[0] = \dot{y}[0] = \dot{\theta}[0] = \dot{\phi}[0] = \dot{\alpha}[0] = 0$$

With the following inputs:

$$\alpha_d = 0.1t$$

and  $d(t)$  is represented in Fig. 5.4 with  $\dot{d}(t) = 0.15$

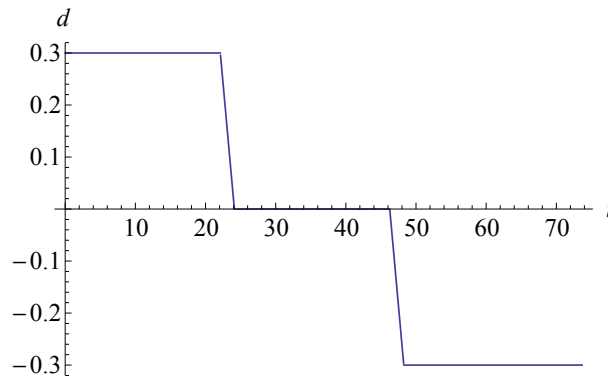


Figure 5.4: The corresponding function  $d(t)$  for the following set of commands:  $\frac{\pi}{8}\text{rad}$ ,  $0.5\text{m}$ ,  $-\frac{\pi}{8}\text{rad}$ .

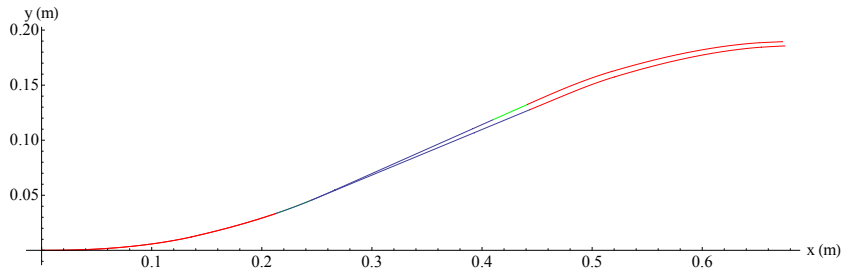


Figure 5.5: Simulation 1: a comparison showing both the real (top) and perfect (bottom) dubins curves.

We can clearly notice from Fig. 5.5 that the final position of the robot has shifted slightly both backwards and upwards when including the phase transitions in  $d(t)$ . The difference in the  $x$  direction is less than 1.5%, while the difference in the  $y$  direction is about 5%.

For our second simulation shown in Fig. 5.7, we study the effect of increasing the straight line segment on the final position of the robot. The set of commands used for the open-loop dubins curve is:

1. Turn by  $\frac{\pi}{8}$ rad
2. Move in straight line for 1.5m
3. Turn by  $-\frac{\pi}{8}$ rad

with the same initial conditions used in Simulation 1, and  $d(t)$  is represented in Fig. 5.6 with  $\dot{d}(t) = 0.15$

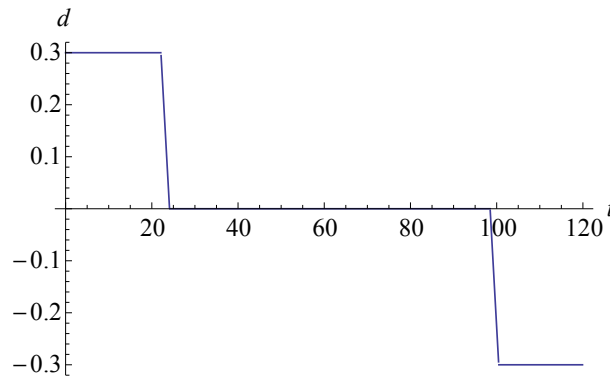


Figure 5.6: The corresponding function  $d(t)$  for the following set of commands:  $\frac{\pi}{8}$ rad, 1.5m,  $-\frac{\pi}{8}$ rad.

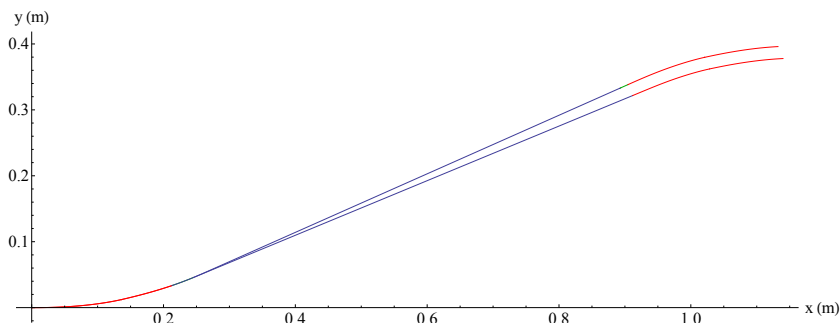


Figure 5.7: Simulation 2: a comparison showing both the real (top) and perfect (bottom) dubins curves.

In this second simulation, we can notice from Fig. 5.7 that the difference in the  $x$  direction is about 1.7%, while the difference in the  $y$  direction is about 5%, which means that the error has remained almost the same compared to Simulation 1.

In our third simulation, we study the effect of increasing the angle of curvature on the final position of the robot. The set of commands used for the open-loop dubins curve is:

1. Turn by  $\frac{\pi}{4}$ rad

2. Move in straight line for 0.5m

3. Turn by  $-\frac{\pi}{4}$ rad

with the same initial conditions used in Simulation 1, and  $d(t)$  is represented in Fig. 5.8 with  $\dot{d}(t) = 0.15$

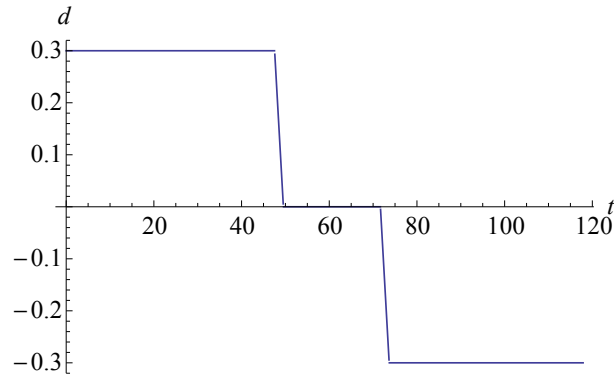


Figure 5.8: The corresponding function  $d(t)$  for the following set of commands:  $\frac{\pi}{4}$ rad, 0.5m,  $-\frac{\pi}{4}$ rad.

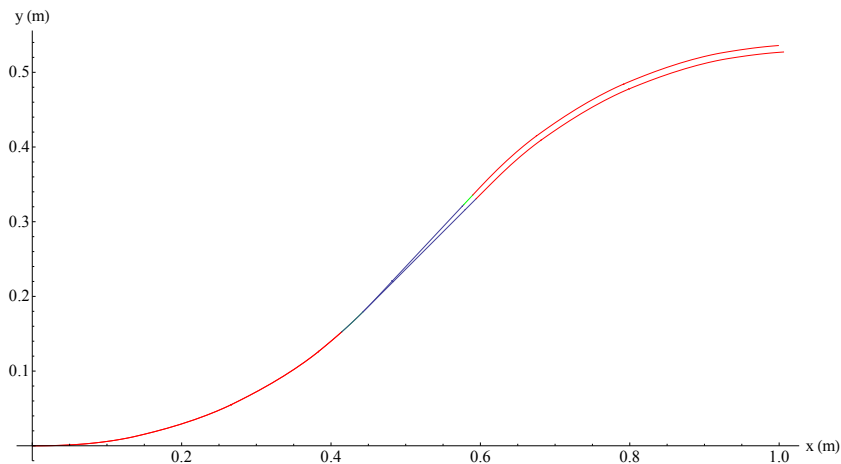


Figure 5.9: Simulation 3: a comparison showing both the real (top) and perfect (bottom) dubins curves.

In the third simulation, we can notice from Fig. 5.9 that the difference in the  $x$  direction is about 1%, while the difference in the  $y$  direction is about 2% (compared to simulation 1), which means that the error is about the same for both  $x$  and  $y$  directions.

In our fourth simulation, we study the effect of having three curvatures on the final position of the robot. The set of commands used for the open-loop dubins curve is:

1. Turn by  $\frac{\pi}{2}$ rad
2. Turn by  $\frac{-\pi}{2}$ rad
3. Turn by  $\frac{\pi}{2}$ rad

with the same initial conditions used in Simulation 1, and  $d(t)$  is represented in Fig. 5.10 with  $\dot{d}(t) = 0.15$

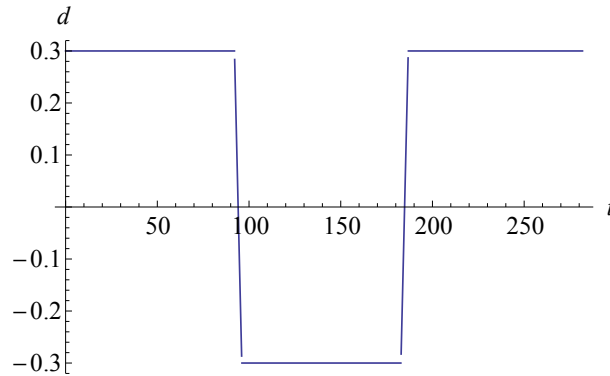


Figure 5.10: The corresponding function  $d(t)$  for the following set of commands:  $\frac{\pi}{2}$ rad,  $\frac{-\pi}{2}$ rad,  $\frac{\pi}{2}$ rad.

In the fourth simulation, we can notice from Fig. 5.11 that the difference in the  $x$  direction is about 5.5%, while the difference in the  $y$  direction is also about 5.5%. These errors are greater than the ones obtained with the previous configurations.

In our fifth and final simulation, we study the effect of increasing the curvatures angles on the final position of the robot. The set of commands used for the open-loop dubins curve is:

1. Turn by  $\frac{\pi}{2}$ rad
2. Turn by  $-\pi$ rad
3. Turn by  $\pi$ rad

with the same initial conditions used in Simulation 1, and  $d(t)$  is represented in Fig. 5.12 with  $\dot{d}(t) = 0.15$

In the fifth simulation, we can notice from Fig. 5.13 that the difference in the  $x$  direction is almost 0%, while the difference in the  $y$  direction is about 33%.

Overall, we can conclude that the phase transitions of the function  $d(t)$ , with a constant value of  $\dot{d}(t)$ , will have a varying effect on the final position of the robot depending on the set of commands used for the open-loop configuration. Therefore, a mathematical equation should be developed, as part of our future

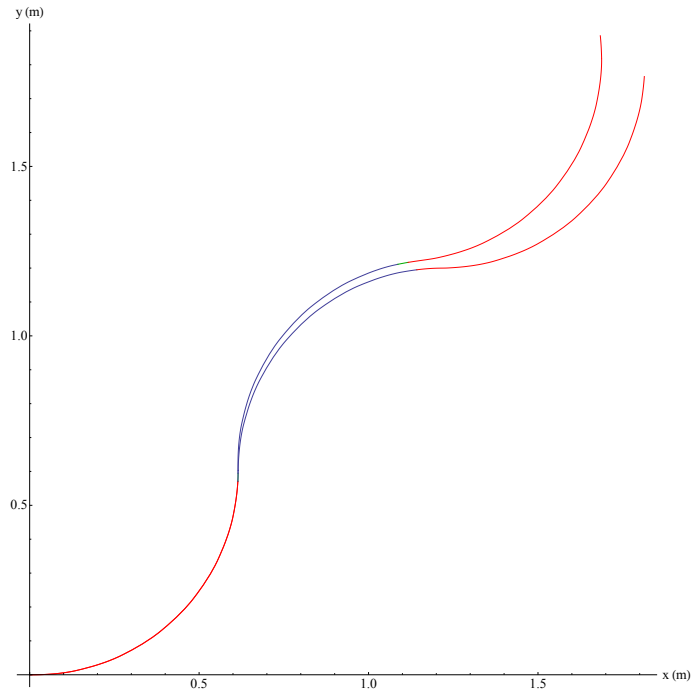


Figure 5.11: Simulation 4: a comparison showing both the real (top) and perfect (bottom) dubins curves.

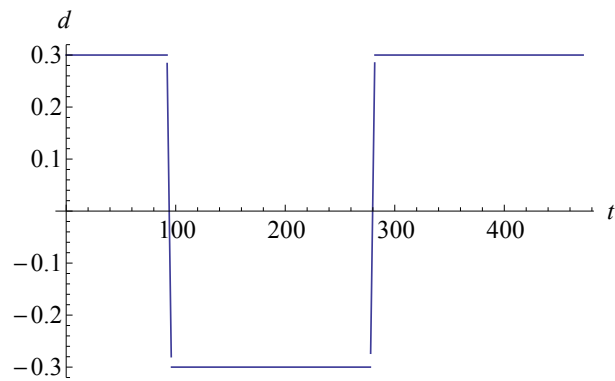


Figure 5.12: The corresponding function  $d(t)$  for the following set of commands:  $\frac{\pi}{2}\text{rad}$ ,  $-\pi\text{rad}$ ,  $\pi\text{rad}$ .

work, to determine and calculate the error generated by the transitions phases, which will enable us to devise a closed-loop control strategy to guide the robot to a predefined final position.

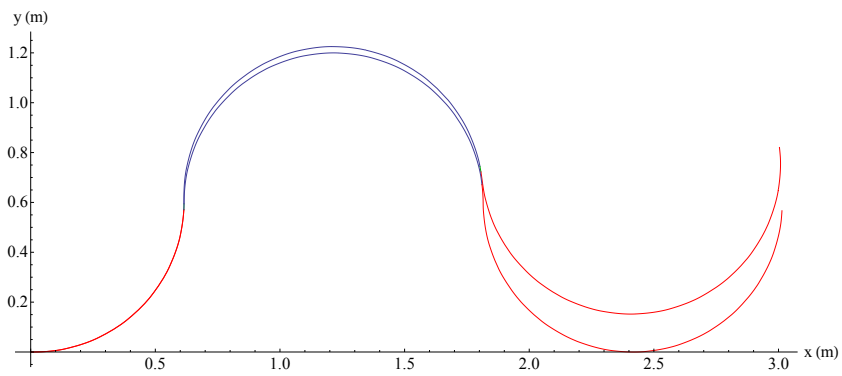


Figure 5.13: Simulation 5: a comparison showing both the real (top) and perfect (bottom) dubins curves.

# Chapter 6

## Conclusion

In this thesis, we proposed a new design for a mobile wheeled pendulum robot with variable-diameter wheels connected to the same shaft and controlled by a single motor to drive and steer the base. The kinetostatic and dynamic analysis of the robot were studied. The kinetostatic results show that the robot can be modelled as a vertical rolling disk with a pendulum. Based on this conclusion, the simplified model is finally used in the dynamic analysis to obtain the equations of motion that predict the trajectory of the robot. Finally, the derived equations of motion are used to study the motion planning problem of the robot by applying Dubins curve.

As part of our future work, we will study the effects of the spoked wheels shape on the systems dynamics, the motion planning problem of the robot and devise a closed-loop control strategy to drive the robot from point A to point B using the shortest path by applying Dubins theorem [22]. Moreover, a prototype of the robot will be build and tested, and hence experimental results will be used to optimize and refine the model.



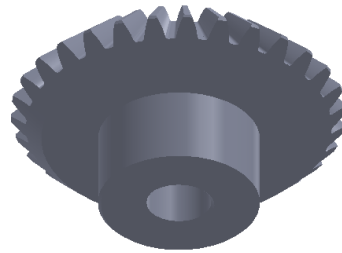
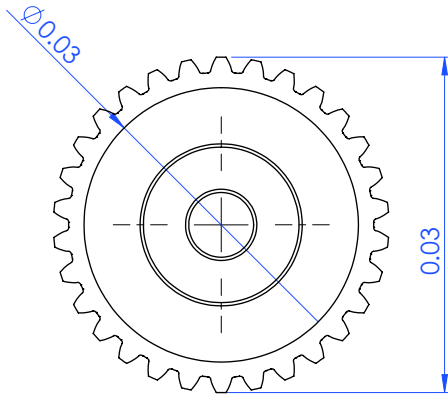
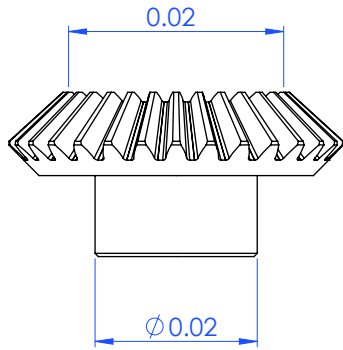
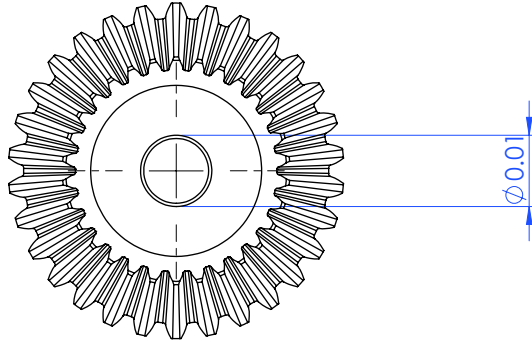
# Appendix A

## Abbreviations

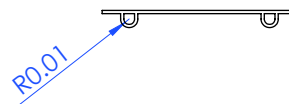
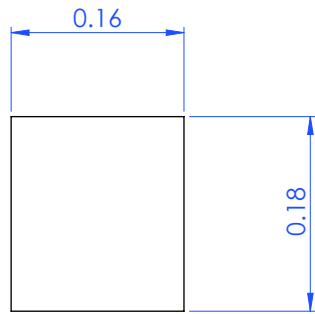
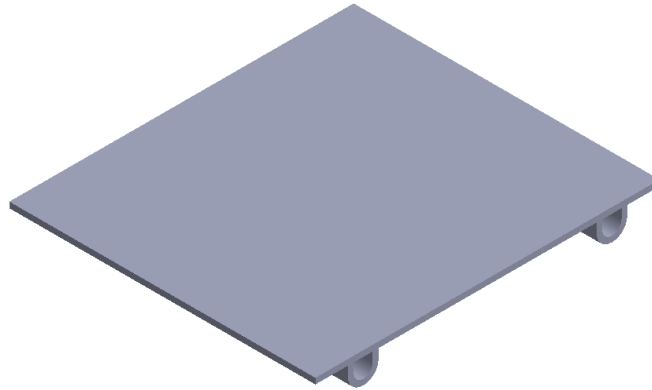
IMPASS	Intelligent Mobility Platform with Active Spoke System
MWP	Mobile Wheeled Pendulum

# Appendix B

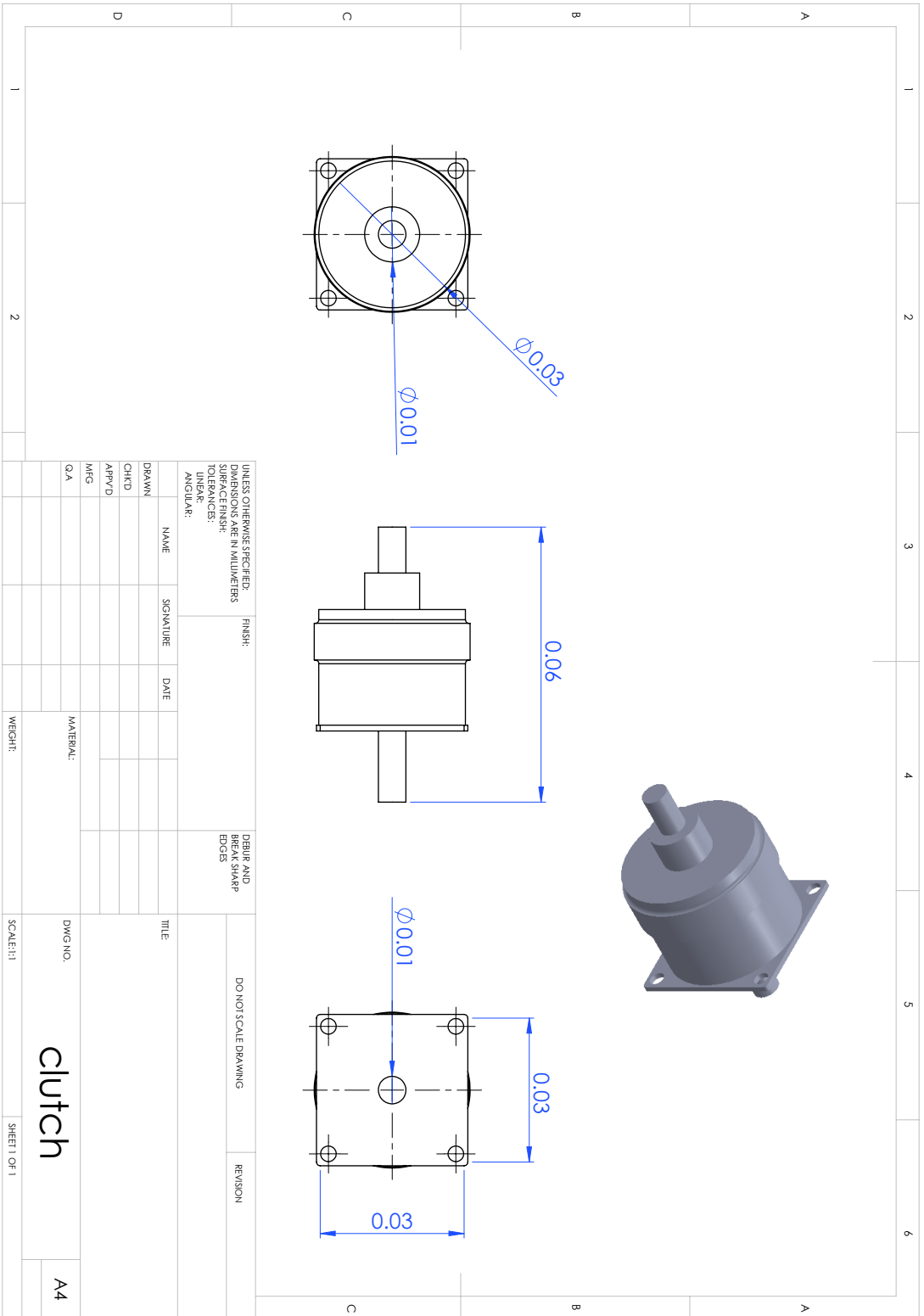
## Design Drawings



UNLESS OTHERWISE SPECIFIED: DIMENSIONS ARE IN MILLIMETERS SURFACE FINISH: TOLERANCES: LINEAR: ANGULAR:				FINISH:	DEBUR AND BREAK SHARP EDGES	DO NOT SCALE DRAWING	REVISION
DRAWN	NAME	SIGNATURE	DATE			TITLE:	
CHKD							
APPV'D							
MFG							
Q.A					MATERIAL:	DWG NO. <b>Bevel_gear_motor</b> A4	
					WEIGHT:	SCALE:1:1	SHEET 1 OF 1



UNLESS OTHERWISE SPECIFIED: DIMENSIONS ARE IN MILLIMETERS		FINISH:		DEBUR AND BREAK SHARP EDGES		DO NOT SCALE DRAWING		REVISION	
SURFACE FINISH:									
TOLERANCES:									
LINEAR:									
ANGULAR:									
	NAME	SIGNATURE	DATE			TITLE:			
DRAWN									
CHK'D									
APP'VD									
MFG									
Q.A					MATERIAL:	DWG NO.	Carriage		A4
					WEIGHT:	SCALE:1:5	SHEET 1 OF 1		



UNLESS OTHERWISE SPECIFIED,  
 DIMENSIONS ARE IN MILLIMETERS  
 SURFACE FINISH:  
 TOLERANCES:  
 LINEAR:  
 ANGULAR:

FINISH:  
 DEBUR AND  
 BREAK SHARP  
 EDGES

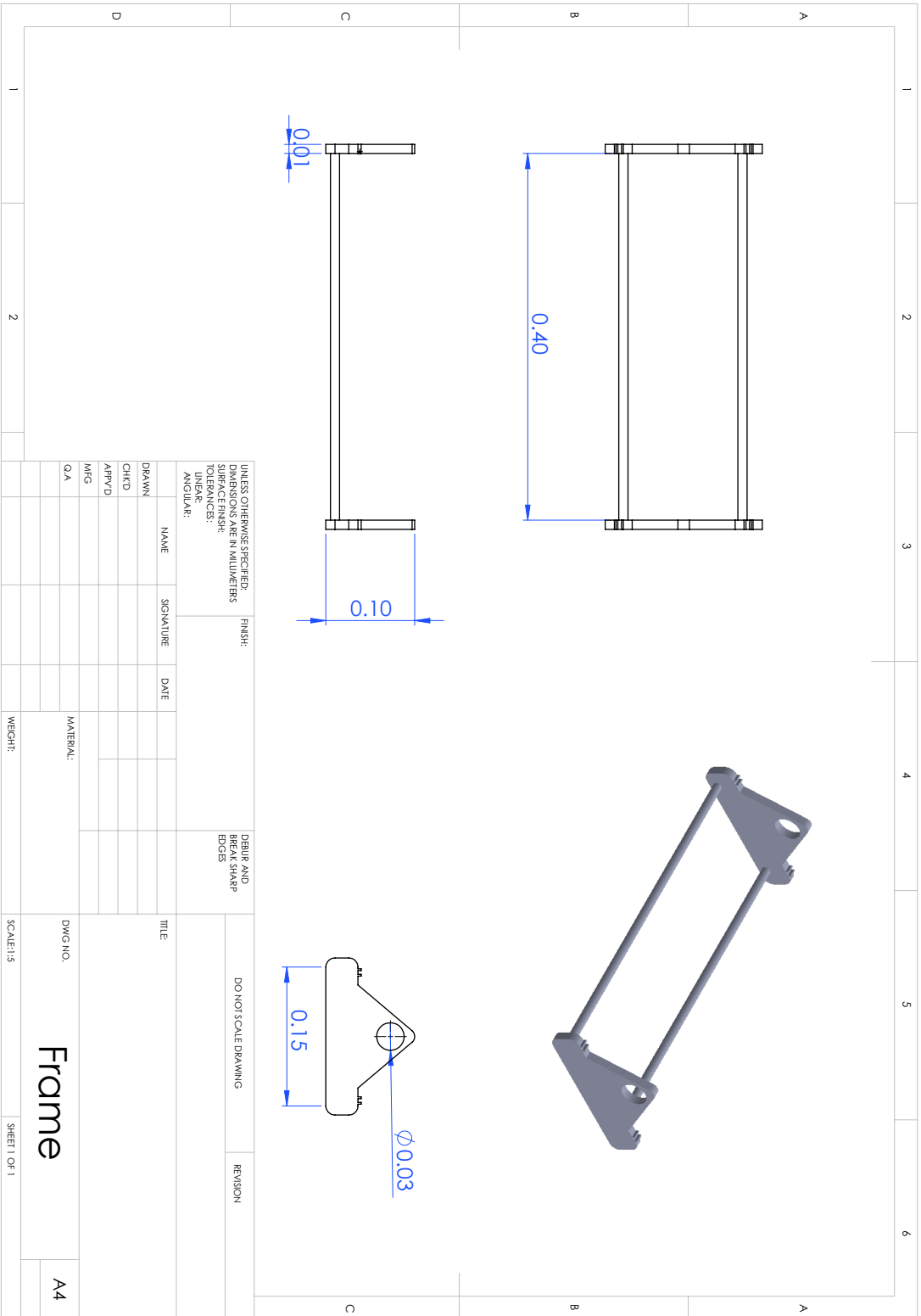
DO NOT SCALE DRAWING

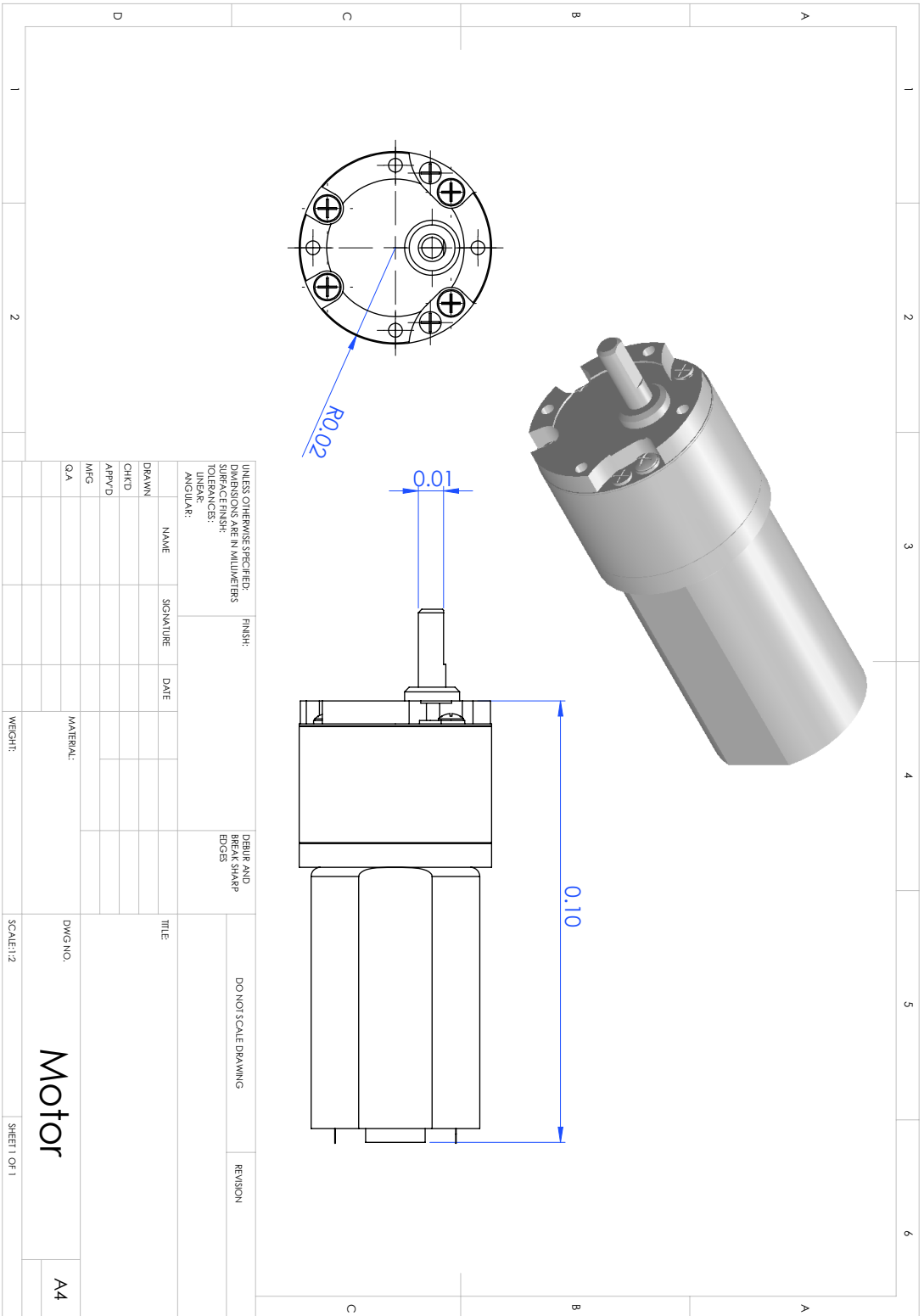
REVISION

NAME	SIGNATURE	DATE
DRAWN		
CHECKED		
APP'VD		
MFG		
QA		

TITLE	DWG NO.	SCALE: 1:1	SHEET 1 OF 1
	clutch		

A4





UNLESS OTHERWISE SPECIFIED,  
DIMENSIONS ARE IN MILLIMETERS  
TOLERANCES:  
LINEAR:  
ANGULAR:

DEBUR AND  
BREAK SHARP  
EDGES

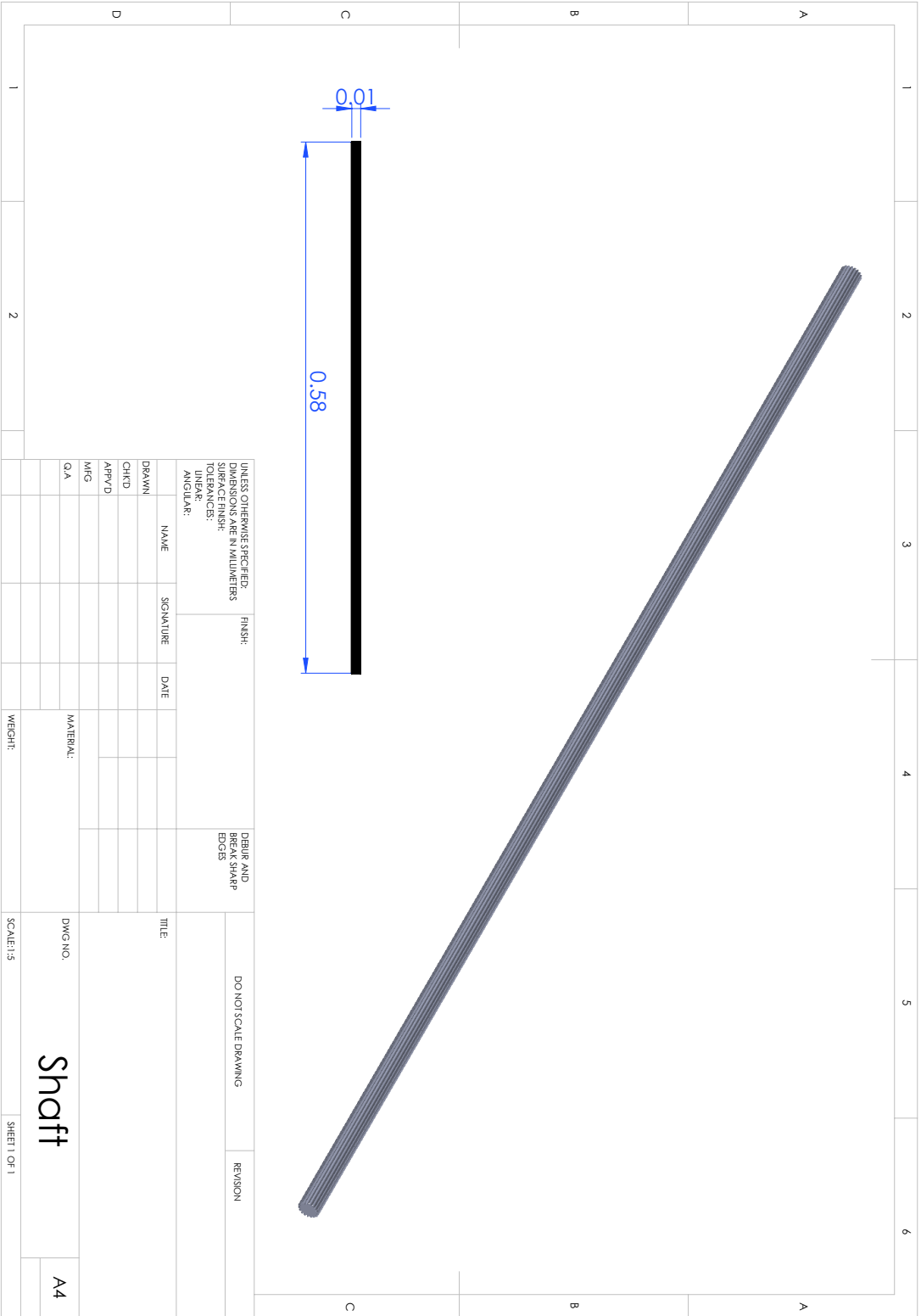
DO NOT SCALE DRAWING

REVISION

NAME	SIGNATURE	DATE	TITLE
DRAWN			
CHKD			
APP'D			
MFG			
QA			
MATERIAL:			DWG NO.
WEIGHT:			<b>Motor</b>
SCALE: 1:2			SHEET 1 OF 1

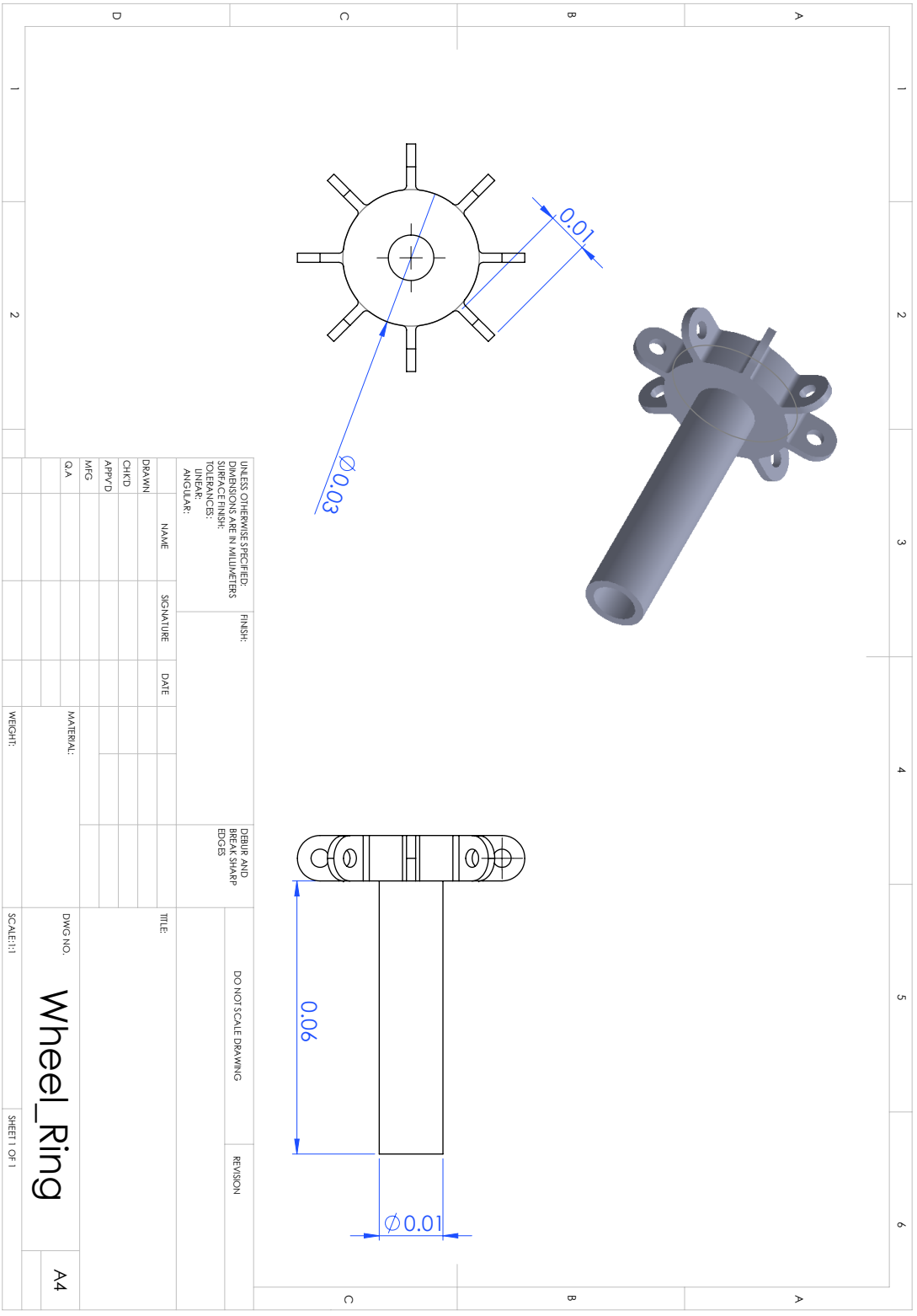
**Motor**

A4



UNLESS OTHERWISE SPECIFIED: DIMENSIONS ARE IN MILLIMETERS		FINISH:		DEBUR AND BREAK SHARP EDGES	
SURFACE FINISH:					
TOLERANCES:					
UNLESS INDICATED:					
ANGULAR:					
DRAWN	NAME	SIGNATURE	DATE	TITLE:	DO NOT SCALE DRAWING
CHK'D					REVISION
APP'VD					
MFG					
G/A					
MATERIAL:				DWG NO.	<b>Shaft</b>
WEIGHT:				SCALE: 1:15	
					A4
SHEET 1 OF 1					





UNLESS OTHERWISE SPECIFIED,  
 DIMENSIONS ARE IN MILLIMETERS  
 SURFACE FINISH:  
 TOLERANCES:  
 LINEAR:  
 ANGULAR:

FINISH:  
 DEBUR AND  
 BREAK SHARP  
 EDGES

DO NOT SCALE DRAWING

REVISION

NAME	SIGNATURE	DATE	TITLE
DRAWN			
CHKD			
APP'VD			
MFG			
QA			

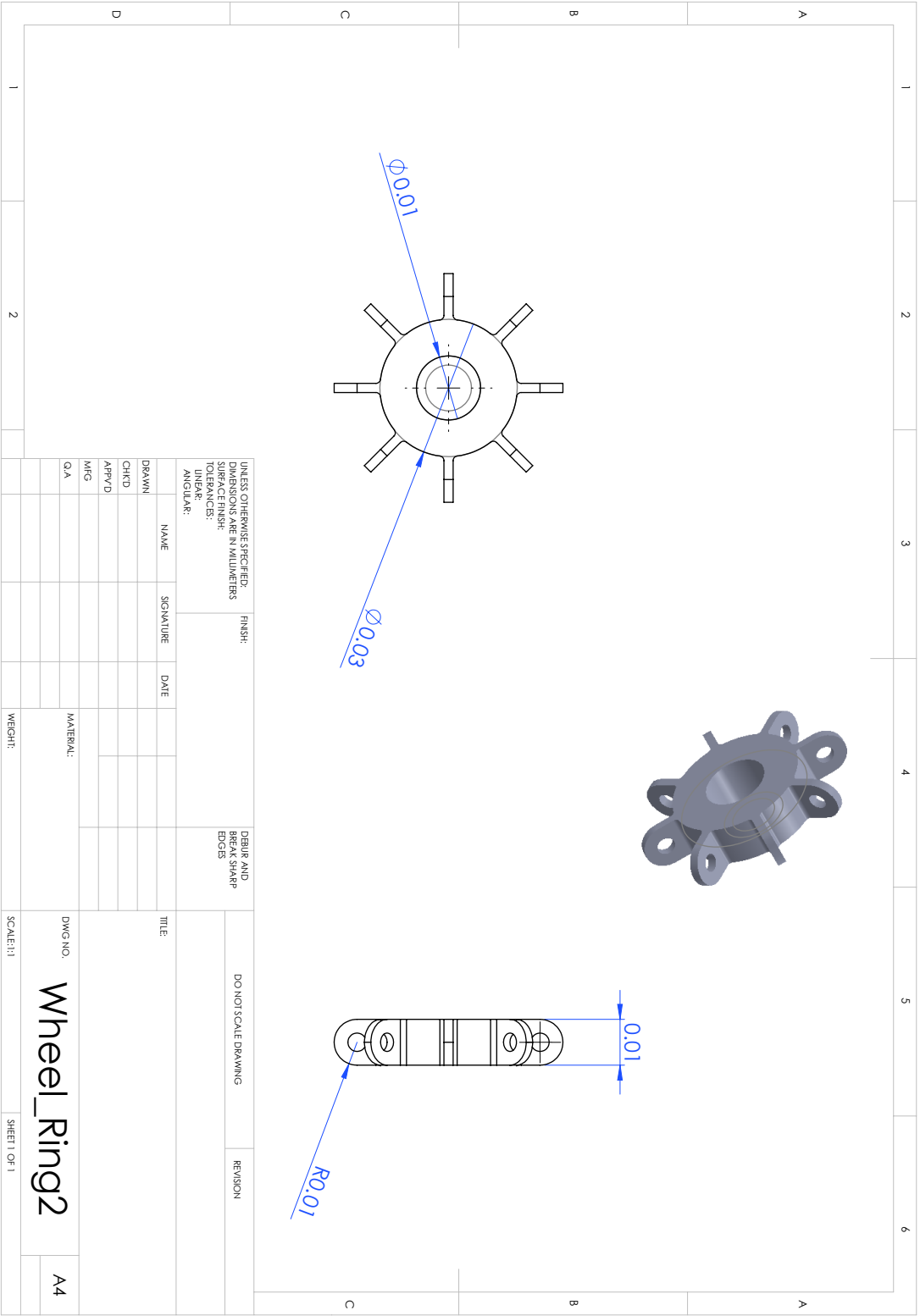
  

MATERIAL:	
WEIGHT:	

DWG NO.	<b>Wheel_Ring</b>
SCALE: 1:1	
SHEET 1 OF 1	

A4



UNLESS OTHERWISE SPECIFIED:  
 DIMENSIONS ARE IN MILLIMETERS  
 SURFACE FINISH:  
 TOLERANCES:  
 UNITS:  
 ANGLES:

FINISH:  
 DEBUR AND  
 BREAK SHARP  
 EDGES

DO NOT SCALE DRAWING

REVISION

TITLE:

NAME	SIGNATURE	DATE
DRAWN		
CHK'D		
APP'D		
MFG		
QA		

MATERIAL:

WEIGHT:

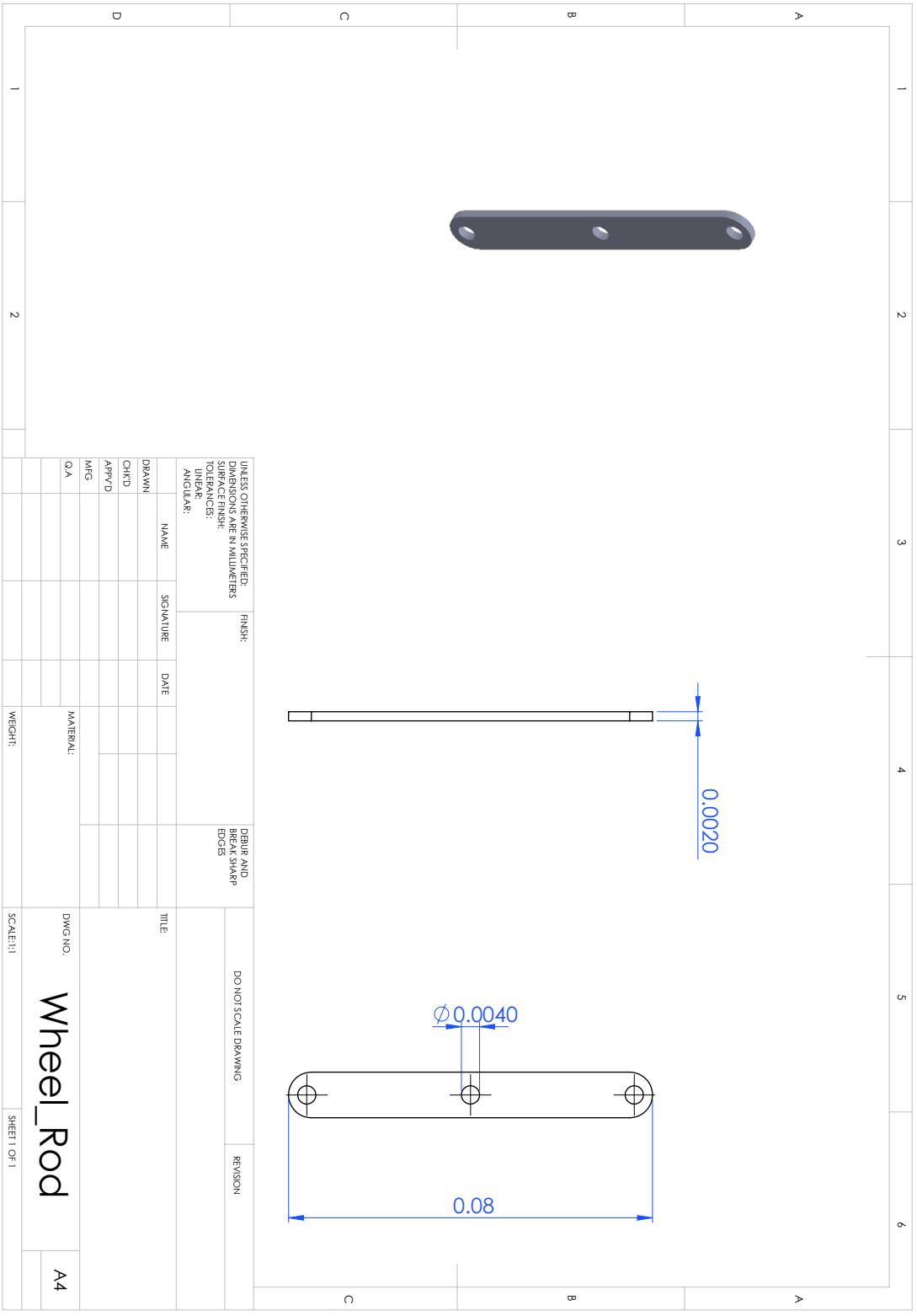
DWG NO.

Wheel\_Ring2

A4

SCALE:1:1

SHEET 1 OF 1



UNLESS OTHERWISE SPECIFIED,  
DIMENSIONS ARE IN MILLIMETERS  
TOLERANCES:  
LINEAR:  
ANGULAR:

FINISH:

DEBUR AND  
BREAK SHARP  
EDGES

DO NOT SCALE DRAWING

REVISION

DRAWN	NAME	SIGNATURE	DATE
CHKD			
APP'VD			
MFG			
QA			

TITLE

DWG NO.

Wheel\_Rod

A4

WEIGHT:

SCALE: 1:1

SHEET 1 OF 1

# Bibliography

- [1] wordpress, “Kuka robot.” <http://roboerectus.wordpress.com/>.
- [2] wikimedia, “Variable-diameter wheel.” <http://commons.wikimedia.org/wiki/File:Variable-diameter-wheel.png>, Dec. 2012.
- [3] University of Minnesota, “Center for distributed robotics.” <http://distrob.cs.umn.edu/scout.php>, Dec. 2012.
- [4] Y. Xiaojiang, G. Feng, X. Guoyan, and C. Ying, “Variable-diameter mobile platform chassis characteristics analysis,” in *Int. Conf. New Technology Agricultural Engineering (ICAE)*, pp. 166–169, May 2011.
- [5] L. Zheng, P. Zhang, Y. Hu, G. Yu, Z. Song, and J. Zhang, “A novel high adaptability out-door mobile robot with diameter-variable wheels,” in *IEEE Int. Conf. Information and Automation (ICIA)*, pp. 169–174, June 2011.
- [6] C. Grand, P. Bidaud, and N. Jarrass, “Design of an innovative unfoldable wheel with contact surface adaptation mechanism for planetary rovers,” in *Proc. 9th ESA Workshop Advanced Space Technologies for Robotics and Automation (ASTRA)*, Jan. 2006.
- [7] K. Nagatani, M. Kuze, and K. Yoshida, “Development of transformable mobile robot with mechanism of variable wheel diameter,” *J. Robot. Mechatron.*, vol. 19, pp. 252–253, Mar. 2007.
- [8] J. Angeles, *Fundamentals of Robotic Mechanical Systems: theory, Methods, and Algorithms*, vol. 124. Springer, 4th ed., 2014.
- [9] F. Grasser, A. D’arrigo, S. Colombi, and A. Rufer, “JOE: a mobile, inverted pendulum,” *IEEE Trans. Industrial Electronics*, vol. 49, no. 1, pp. 107–114, Feb. 2002.
- [10] benjahedley, “Ban public transport. buy segways..” <http://co2calculator.wordpress.com/2008/10/22/ban-public-transport-buy-segways-save-the-earth-with-the-help-of-the-cheeky-girls/>, Oct. 2008.

- [11] wikimedia, “Triple rotacaster.” <http://upload.wikimedia.org/wikipedia/commons/e/e3/Triple-Rotacaster-commercial-industria-omni-wheel.jpg>.
- [12] Microrobo, “Stainless-steel mecanum wheel.” <http://www.microrobo.com/images/203mm-stainless-steel-mecanum-wheel-right-with-rubber-rollers-14150-3.jpg>.
- [13] H. G. Nguyen, J. Morrell, K. D. Mullens, A. B. Burmeister, S. Miles, N. Farington, K. Thomas, and D. Gage, “Segway robotic mobility platform,” in *Proc. SPIE 5609: Mobile Robots XVII*, pp. 207–220, Oct. 2004.
- [14] dlife, “Package dlife.robot.pioneer.” <http://users.dickinson.edu/brought/dlife/javadoc/doc/dlife/robot/pioneer/package-summary.html>.
- [15] A. Mobilerobots, “Peoplebot.” <http://www.mobilerobots.com/ResearchRobots/PeopleBot.aspx>, 2013.
- [16] Robotic Intelligence Lab, “Robotic intelligence lab.” <http://www.robot.uji.es/lab/plone/robots>, May 2010.
- [17] Yenra, “Robots.” <http://www.yenra.com/security-robot/>, Apr. 2004.
- [18] D. Laney and D. W. Hong, “Three-dimensional kinematic analysis of the actuated spoke wheel robot,” *30th ASME Mechanisms and Robotics Conference (MR)*, September 2006.
- [19] I. Burt, T. Dahlin, B. Kratochvil, C. McMillen, B. Nelson, N. Papanikolopoulos, P. E. Rybski, K. Stubbs, D. Waletzko, and K. B. Yesin, “Mobility enhancements to the scout robot platform,” in *Proc. IEEE Int. Conf. Robotics and Automation (ICRA)*, pp. 1069–1074, 2002.
- [20] Y. Xiaojiang, G. Feng, X. Guoyan, and C. Ying, “Variable-diameter mobile platform chassis characteristics analysis,” in *Proc. Int. Conf. New Technology of Agricultural Engineering (ICAE)*, pp. 166–169, May 2011.
- [21] L. Zheng, P. Zhang, Y. Hu, G. Yu, Z. Song, and J. Zhang, “A novel high adaptability out-door mobile robot with diameter-variable wheels,” in *Proc. IEEE Int. Conf. Information and Automation (ICIA)*, pp. 169–174, June 2011.
- [22] L. E. Dubins, “On curves of minimal length with a constraint on average curvature, and with prescribed initial and terminal positions and tangents,” *Am. J. Math.*, vol. 79, pp. 497–516, July 1957.